An insight on the key factors influencing the accuracy of the Actuator Line Method for use in vertical-axis turbines: limitations and open challenges

Omar S. MOHAMED[1a], Pier Francesco MELANI[1b], Francesco BALDUZZI[1c], Giovanni FERRARA[1d], Alessandro BIANCHINI[1e*]

[1)] Department of Industrial Engineering, Università degli Studi di Firenze
Via di Santa Marta 3, 50139, Firenze, Italy
Phone +39 055 275 8773
Fax + 39 055 275 8755
* alessandro.bianchini@unifi.it

Abstract

Darrieus vertical-axis turbines are known for their complex aerodynamics connected to the continuous change in the angle of attack experienced by the blades, which often exceeds the static stall limit. Low fidelity tools such as the Blade Element Momentum Theory have been shown lately not to provide sufficient levels of accuracy, while the medium-fidelity Actuator Line Method (ALM) has been increasingly applied to Darrieus rotors. In this method, the blade-flow interaction is modeled as an equivalent momentum loss calculated introducing equivalent aerodynamic forces into the computed Computational Fluid Dynamics (CFD) domain. This strongly reduces the computational cost in comparison to blade-resolved CFD, allowing ALM to be used in three-dimensional problems, e.g., multiple rotors, floating offshore, etc. While several corrections and guidelines have been recently proposed to tailor ALM to Darrieus turbines, issues are still open on how to improve accuracy.

The present study aims at assessing to what extent the three main factors of the ALM theory, namely the quality of input polar, the dynamic stall modeling, and the force insertion in the domain, influence the overall accuracy of the method. In particular, this unprecedented understanding is enabled by the novel use of a "frozen ALM", i.e., an ALM method fed by the aerodynamic forces calculated by blade-resolved CFD, which allowed to separate the contributions coming from airfoil performance analysis and force projection in the domain. Based on the results, three main important conclusions are drafted out: i) for high and medium tip-speed ratios, provided that the aerodynamic forces are correct, the ALM method is able to generate extremely accurate solutions of the flow field, almost equivalent to blade-resolved CFD; ii) the relevance of the kernel's shape and smearing function is largely overestimated and current knowledge is adequate for the model to be set; iii) a better dynamic stall model is indeed the real key factor that could lead to an improvement of the ALM accuracy.

Keywords: Actuator Line Model (ALM), Darrieus, Vertical Axis Wind Turbine (VAWT), Hydrokinetic Turbines, Computational Fluid Dynamics (CFD), Dynamic stall

Nomenclature

Latin

A_M	Berg model tuning constant	[-]
c	Chord length	[m]
C_D	Drag coefficient	[-]

C_L	Lift coefficient	[-]
C_N	Normal force coefficient	[-]
C_T	Tangential force coefficient	[-]
D	Turbine diameter	[m]
E^2	Mean square error	[-]
F_b	Body force term	[N]
F_N	Normal force	[N]
F_T	Tangential force	[N]
F_X	X-direction force	[N]
F_Y	Y-direction force	[N]
h	Cell characteristic dimension	[m]
n	Number of blades	[-]
u	X-velocity	[m/s]
v	Y-velocity	[m/s]
V_∞	Undisturbed wind velocity in axial direction	[m/s]
V_{rel}	Relative wind velocity	[m/s]

Greek

ρ	Fluid density	[kg/m^3]
β	Gaussian kernel width	[m]
β_c	Gaussian kernel width in chord direction	[m]
β_t	Gaussian kernel width in thickness direction	[m]
θ	Azimuth Angle	[deg.]
ω	Angular speed	[rad/s]

Abbreviations and Acronyms

ALM	Actuator line method
aniso	Anisotropic Gaussian
AoA	Angle of attack [deg.]
BEM	Blade element momentum
BSC	Blade spoke connection
CFD	Computational fluid dynamics
CSS	Cubic spline smoothing
FOWT	Floating offshore wind turbine
GG	Anisotropic Gaussian-Gumbel
HAWT	Horizontal axis wind turbine
HKT	Hydrokinetic turbine
iso	Isotropic Gaussian
LES	Large eddy simulation
PIV	Particle image velocimetry
SST	Shear stress transport
TSR	Tip Speed Ratio
URANS	Unsteady Reynolds-averaged Navier-Stokes

1. Introduction

The performance of a Darrieus turbine is characterized by the instantaneous variation of the angle of attack (AoA), which can even exceed the static stall limit at some azimuthal positions, thus triggering the dynamic stall phenomenon [1]. This issue is more relevant at low and medium tip-speed ratios (TSRs) [2]. Nevertheless, some specific features associated with the Darrieus turbine functioning principle and architecture make it particularly attractive for some special applications, e.g., multiple-rotor arrays [3], Floating Offshore Wind Turbines (FOWTs) [4], urban wind power generation [5], and energy generation from small watercourses [6]. On the other hand, the intrinsic complexity of blade aerodynamics has the main drawback of making their simulation and design very complex. In particular, recent studies have pointed out that engineering methods like the Blade Element Momentum (BEM) theory, although empowered by recent modifications that enhanced their accuracy, can hardly capture some of the involved physics, paving the way for a larger use of higher fidelity techniques, among which Computational Fluid Dynamics (CFD) plays a key role [7]–[9]. However, although using blade-resolved CFD gives an accurate solution to the Darrieus rotor flow field and load estimations, it is still computationally prohibitive for three-dimensional analyses due to strict requirements in terms of mesh and timestep accuracy [10]. To improve on design, a more reliable, but computationally-affordable, simulation tool is therefore needed. To this end, hybrid simulation methods are increasingly welcome. In particular, Sørensen and Shen [11] first introduced a few years ago the concept of the Actuator Line Method (ALM) for Horizontal Axis Wind Turbines (HAWTs) as a realistic alternative between the blade-resolved CFD and BEM. The ALM is based on inserting the lift and drag forces into momentum equations as body forces distributed on a line that represents the blade. Thus, there is no need to resolve the blade boundary layer, which makes the ALM computationally far less expensive compared to the conventional blade-resolved CFD. The ALM has been extensively developed in the last few years for HAWTs to account for tip and root losses [12] and chord length variation [13]. Other works have validated the use of ALM coupled with Large Eddy Simulation (LES) in advanced applications such as analysis of near and far wakes [14] as well as the wind farm wake interaction with the atmospheric boundary layer [15].

Moving from these successful study cases, few studies also discussed the use of ALM for Darrieus rotors. Shamsoddin and Porte-Agel [16] applied the ALM to a Darrieus wind turbine for the first time to analyze the wakes using LES. Potential sources of discrepancies between simulated and measured data were attributed to the limitations in the numerical model, experimental errors in measurements, and inaccuracies in the tabulated airfoil data. Bachant et al. [17] found that RANS ALM overpredicts the power coefficient at high tip-speed ratios, ascribing the sources of error to either unmodelled bodies (e.g., drag due to spokes) or limitations in the aerodynamic data (e.g., the effect of virtual camber or dynamic stall). Mendoza et al. [18] compared the ALM predictions of a Darrieus turbine flow field with experimental data and attributed the source of mismatch to the oversized kernel width β, as well as to the sensitivity on the predicted aerodynamic forces. Zhao et al. [19] showed that RANS ALM overpredicts the thrust coefficient at almost all tip-speed ratios; this has been explained by the authors as a cause of the blockage effect in the solution domain, in addition to the lack of data regarding the turbulence intensity of experimental results. Mendoza and Goude [20] evaluated the ALM sensitivity to the aerodynamic coefficients by using two different sets of polar data, one measured experimentally [21] that showed underestimated power coefficient values, and the other exported from XFoil [22] that showed an overestimation of the power coefficient at low tip-speed ratios. More recently, Melani et al. [23], [24] proposed a number of submodels and corrections to tailor the ALM for use in Darrieus

VAWTs, obtaining notable improvements in the overall accuracy, while still seeing some general overestimation of the performance, especially in the dowind region of the rotor.

Based on this background, one can say that the implementation of the ALM for Darrieus turbines still lacks a detailed investigation to determine the sources of discrepancy versus CFD, so as to understand the areas where improvements can be made. Generally speaking, three main issues are currently deemed to be responsible for existing lacks in modeling fidelity, i.e.: i) the quality of airfoil polar data and its ad hoc correction models [25], [26], e.g., flow curvature effects; ii) the dynamic stall modeling, which is especially critical at low and medium tip-speed ratios [27]; iii) the insertion of the body forces into the domain, which is usually through the standard *isotropic two-dimensional Gaussian kernel* [13]. However, no consensus still exists on the relative impact of each of these effects.

Moreover, it should be noted that while the first and second issues are intrinsically related to the characteristics of Darrieus rotor aerodynamics, the third issue could be relevant also when applying the ALM to a HAWT. This is testified by the fact that the use of a more physically related Gaussian kernel has been suggested lately also for HAWTs. Martínez-Tossas et al. [28] investigated the influence of using a cylindrical anisotropic Gaussian kernel. They concluded that using optimal scales for the kernel widths allows the ALM to resolve small flow structures such as those found near the blade tip. By doing so, the ALM is capable of predicting the blade tip load without using tip loss correction. Cormier et al. [29] studied the effect of the ALM force smearing function, finding that the force projection function does not cause a significant difference in the tip vortex properties, and attributed the accuracy of reproducing the near-wake flow field to the mesh refinement. Churchfield et al. [30] tested an anisotropic Gaussian kernel, observing a more compact body forces distribution and a higher capability of the ALM to capture the tip vortices and their consequent effects more accurately. Martínez-Tossas et al. [31] used an analytical approach for a static airfoil to optimize the scales of the circular and elliptical kernel widths (β_t and β_c). The latter approach was based on comparing the potential flow solution over a Joukowsky airfoil with that of an ALM solution that utilizes the aerodynamic coefficients exported from the former analytical solution, namely the *Frozen ALM*.

1.1 Outline and contribution of the study

The present study is the outcome of a several-year research that the wind energy research group at the University of Florence has been carrying out over the last years focused at making computationally affordable those higher-fidelity methods that could provide the necessary step forward in Darrieus VAWT technology. More specifically, in [1] a novel method to extrapolate the angle of attack on a Darrieus turbine from a CFD-computed flow field. This passage was indeed of capital importance because it represented the only way to get useful benchmarking data from CFD. Thanks also to the information gathered with the new method, in [24] a number of corrections, sub-models and new methods have been presented that allowed tailoring the ALM to Darrieus VAWTs, while leaving some issues open on how to further improve the accuracy of the ALM.

The present study fills these open issues, providing an unprecedented overview on the specific research areas to be addressed to improve the accuracy of this method is highlighted, with particular focus on the actual influence of polar data quality, dynamic stall model, and force insertion function on the load estimation accuracy, as well as on the reproduction of the flow field. This has been achieved by a novel method developed specifically for this study, which is based the application to Darrieus VAWTs of the *Frozen ALM* approach originally introduced by

Martínez-Tossas et al. [31]. As will be shown in the paper, in the newly developed *Frozen ALM* the aerodynamic forces are determined from a blade-resolved CFD, thus enabling the elimination of the uncertainties related to the quality of the polar data or the dynamic stall model. By doing so, any possible discrepancy between the Frozen ALM and the blade-resolved CFD results must be attributed to the kernel function. The possibility of splitting these contributions has never been possible before, thus always leaving doubts on the relative impact of each contribution and on their mutual influence.

Specifically, the objectives of this work are to: i) isolate and investigate the effect of the kernel shape and size; ii) highlight the real influence of the polar data and the dynamic stall modeling on the solution fidelity; iii) evaluate the solution sensitivity to the grid size for each of the evaluated kernel shapes.

Three kernel functions were investigated: isotropic Gaussian (*iso*) [13], anisotropic Gaussian (*aniso*) [32], and anisotropic Gaussian-Gumbel (*GG*) [33]. Unlike the cylindrically shaped isotropic function, the other two non-isotropic Gaussians make the shape of the projected body forces look more similar to the turbine blade. The latter non-isotropic functions have been previously applied to the ALM for HAWTs, but to the best of the authors' knowledge, they have not been studied in the context of Darrieus rotors to date.

The structure of this paper is as follows: In Section 2, details on the geometrical and operational characteristics of the selected test cases are demonstrated. Section 3 outlines the numerical methodology used in the present study, including a brief description of the ALM base formulation, *Frozen ALM* algorithm, and CFD set-up. The results are given in Section 4, where firstly a calibration of the kernel size is made using *Frozen ALM* for a static airfoil, followed by the *Frozen ALM* results for turbine cases. Thereafter, the significance of the kernel size is evaluated using the standard ALM. Then, grid sensitivity analysis is conducted for different kernel shapes. And finally, comparative analyses and remarks are highlighted. Section 5 presents a discussion of the results, emphasizing their relevance to the current state-of-the-art. The conclusions and future work are presented in Section 5.

2. Study cases

To generalize the findings of this study for all Darrieus turbines, i.e. both wind and hydrokinetic ones, two different rotors have been considered, labelled as "*R1000* HKT" and "*R500* VAWT", respectively. Both turbines are of H-Darrieus type. Figure 1 shows a schematic representation of the H-type Darrieus rotor and the performance curves for both *R1000* and *R500* rotors. More details on the geometrical and operational characteristics are shown in Table 1 and 2, respectively.

- *R1000:* industrial two-blade Darrieus HKT, for which multiple design configurations have been investigated in a previous work [6]. It has been also studied in [35], where an investigation on a possible active pitch control strategy has been conducted using ALM. It is also worth remembering that for this rotor data from a high-fidelity, blade-resolved, two-dimensional CFD simulation are available; this dataset was used in the present study both for validation purposes and to obtain the input data needed for the Frozen ALM cases;
- *R500:* real two-blade, H-shaped Darrieus VAWT, tested in different studies [36], [37] in the Open Jet Facility (OJF) at TU Delft. For this machine, both three-dimensional flow fields [36] and azimuthal blade force profiles [37] are available from *ad hoc* post-processing of measured PIV (Particle Image Velocimetry) data. To further support the validation process, two-

dimensional blade-resolved CFD simulations from Melani et al. [38] are also here employed as a benchmark next to experimental measurements.

As apparent, the choice of these rotors for the investigation is justified not only by the quantity and quality of the corresponding available benchmark data, but also by the possibility of generalizing the findings of this paper over a significant range of turbine architectures, solidities, and airfoils. Furthermore, both test cases fall in the low-to-medium solidity range, which is particularly indicated for hybrid simulation models, as their accuracy in fact strongly decreases going towards high-solidity configurations [39]. Furthermore, the choice of the operating conditions (see Table 2) was based on the will of assessing the ALM tool in different modes of operation. For the *R1000*, the optimum TSR of 2.5 was selected, since a significant impact of the dynamic stall model has been proven to exist. On the other hand, a TSR of 4.5 was selected for the *R500*, in which the operation is stable, and the dynamic stall phenomenon is not relevant.

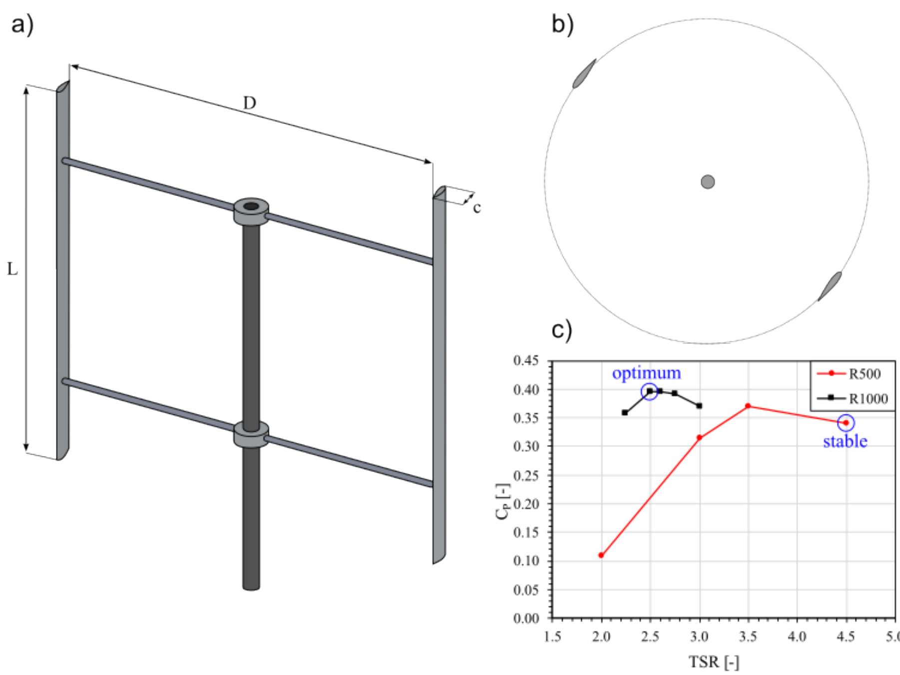

Figure 1 – a) generalized schematic representation of the Darrieus rotor, b) top view schematic of the Darrieus rotor, and c) performance curves of R500 and R1000.

Table 1 - Details of test rotors selected for the investigation.

Dimension	R1000	R500
Number of blades [-]	2	2
Diameter, D [m]	2	1
Chord, c [m]	0.25	0.06
Rotor solidity (Nc/D), σ [-]	0.25	0.12
Airfoil	DU06W200	NACA0018
Blade-spoke connection [x/c]	0.25	0.25

Table 2 – Test operating conditions.

Inlet value	R1000	R500
Tip-speed ratio [-]	2.5	4.5
Inflow fluid [-]	Water	Air
Inflow speed [m/s]	2	9.1
Inflow temperature [°C]	25	20
Turbulence intensity [%]	0.24	0.24

3. Methods

3.1 Actuator Line Method

3.1.1 ALM algorithm

The ALM code used in the present study is an in-house code, tailored specifically for vertical-axis turbines and it has been validated already in previous works [23], [34], [35]. The ALM code is implemented through a custom User Defined Function (UDF) in ANSYS© FLUENT© (version 2020 R2).

In the ALM, lift and drag forces are projected into lines that represent the blades. Thus, no need to model the blade boundary layer. The aerodynamic forces are inserted into the computational domain of the CFD solver as a source term along the blade span. Figure 2 shows a schematic representation of the ALM for a straight-blade Darrieus turbine.

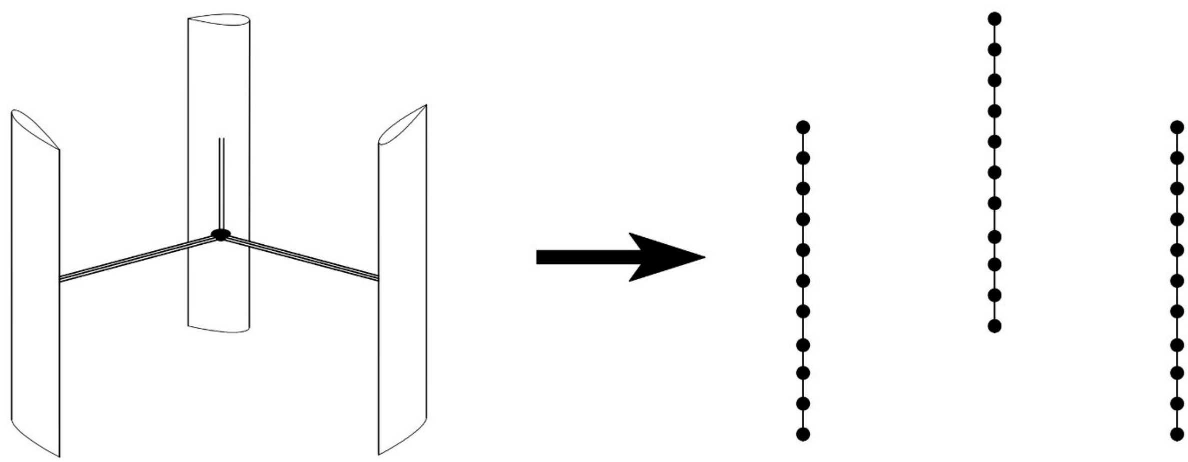

Figure 2 - Schematic representation of the ALM for straight-bladed Darrieus turbine.

The modified governing equations: (1) continuity and (2) momentum reads:

$$\nabla \cdot \vec{V} = 0 \quad (1)$$

$$\frac{D\vec{V}}{Dt} = -\frac{1}{\rho}\nabla p + \upsilon\nabla^2 \cdot V + F_b \quad (2)$$

where $\frac{D\vec{V}}{Dt}$ represents the acceleration and the convection term, $-\frac{1}{\rho}\nabla p$ is the pressure gradient, $\upsilon\nabla^2 \cdot V$ is the diffusion term, and F_b is the inserted body forces term. The body forces are computed using the local aerodynamic forces which read as:

$$F_L = \frac{1}{2}\rho V_{rel} c C_L \tag{3}$$

$$F_D = \frac{1}{2}\rho V_{rel} c C_D \tag{4}$$

where V_{rel} is the relative velocity, C_L and C_D are the coefficients of lift and drag, respectively. Normally, C_L and C_D are obtained using tabulated data based on the local angle of attack *AoA*. Where *AoA* and *W* are determined from velocity sampling each time step. To avoid non-physical discontinuities, the body forces have to be smeared out into the computational domain properly via a regularization kernel. Where $\eta(r)$ is the regularization kernel smearing function, the body forces f_b reads:

$$f_b = f_{2D} \otimes \eta(r) \tag{5}$$

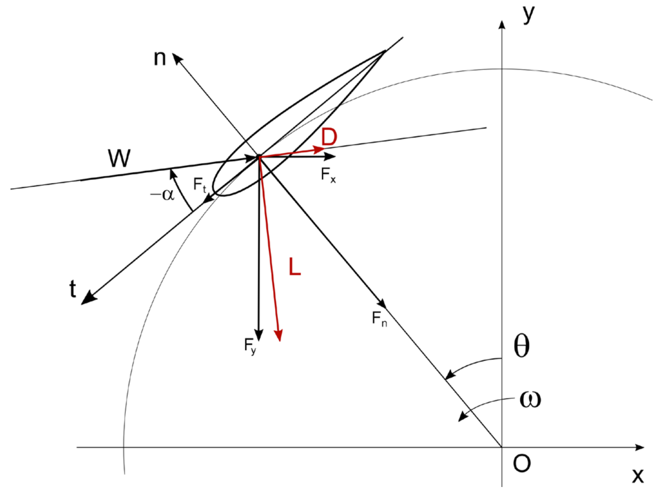

Figure 3 - Conventions adopted for the present study.

The main features of the ALM code used in this study [24] are:

- *Velocity sampling*: The *LineAverage* method is used in this work to sample the local velocity through integral averaging of the undistributed inflow along a circular line around the hypothetical blade, this line has a radius r = 1c and a resolution N = 80 of equally spaced points along the sampling line, as shown in Fig. 4. This method was originally proposed for HAWTs by Jost et al. [40] and has been verified and validated against other methods by the authors in recent works on VAWTs [1], [2]. To minimize the background noise [34], the *LineAverage* method is coupled with low-pass filtering of the sampled data by using a dedicated Cubic Spline Smoothing (CSS) algorithm [41]. At the beginning of each rotor revolution, the latter ad hoc filtering strategy is applied to the AoA signals coming from the previous revolution, therefore, no real-time processing is needed. The smoothed AoA signal is then derived over time and used as an input for the dynamic stall model.

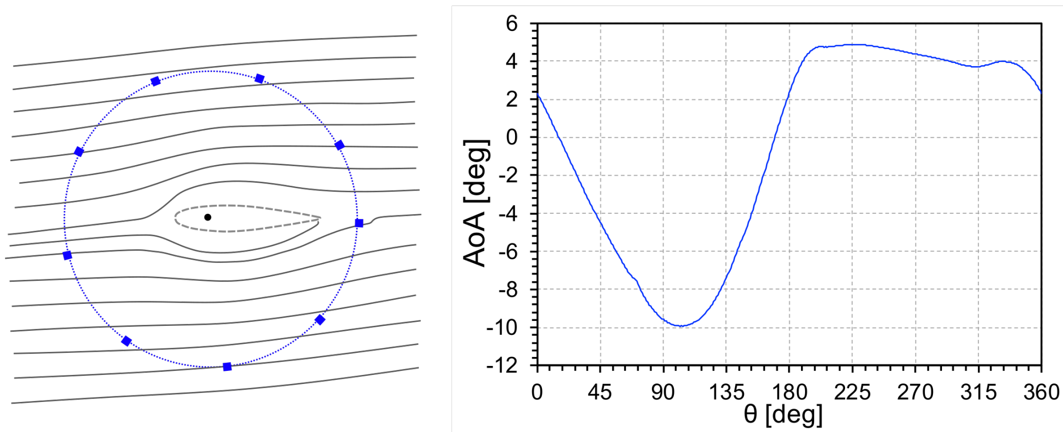

Figure 4 - Schematic comparison between the Tangent and the LineAverage methods.

- *Polar data*: The quality of the polar data plays a vital role in the capability of the ALM code to predict the rotor performance accurately, hence, proper modeling of the flow field around the rotor. For small Darrieus rotors such as the two case studies considered in the current work, the operating range of Reynolds numbers is relatively low. Thus, the influence of laminar separation bubbles on the aerodynamic performance of the airfoil is more relevant. For the R1000 rotor, the pre-stall aerodynamic coefficients were obtained via blade resolved CFD for Re ∈ [7.5×10^5 2×10^6]. The 4-equations γ-Reθ transition model [42] was employed for the closure of the turbulence problem. On the other hand, for the R500 rotor, the pre-stall aerodynamic coefficients were calculated with the viscid panel method software XFoil [22], since a benchmark against more complex methods proved them to be sufficiently robust. Both sets of data have been extended over the deep stall region, i.e. up to AoA=±180°, via the Viterna-Corrigan model [43], as recommended by Bianchini et al. [44] for VAWT applications.
- *Berg dynamic stall model*: To consider the unsteadiness effect on the blade loads, the dynamic stall model from Berg [45] has been used in the ALM code for the test case of *R1000*, employing the formulation proposed in [34]. In brief, the Berg model involves the dynamic effects by introducing a delay in the measured angle of attack that is proportional to the flow reduced frequency via a coefficient γi. It must be noted how the latter, which is given in the model as a semi-empirical function of the airfoil thickness and the freestream Mach number, was treated in this work as a free parameter. The airfoil used in the *R1000* rotor, DU-06-W-200 profile, is in fact way thicker than those tested in the original work of Gormont [46] for the derivation of this correlation. Lift and drag coefficients are eventually obtained as a linear interpolation between the static and dynamic ones, weighted over the constant A_M. In the present work, A_M was set to be 6 and γi to 1.5 based on the dedicated calibrations that were conducted in [35] for the *R1000* rotor. However, as will be discussed later on the study, one should bear in mind that a more effective dynamic stall model is indeed probably the real missing element in VAWT simulation and will deserve attention in the near future, either trying to tune more advanced ones like the Beddoes-Leishman model, or so synthetize new ones specifically tailored for these turbines.

- *Pitching moment and BSC corrections*: It must be noted how, in order to take the flow curvature phenomenon into account in the simulation campaign, the tabulated data for both R1000 and R500 rotors were derived for a virtually cambered airfoil, obtained by proper conformal mapping from the geometric one according to the rotor chord-to-radius ratio c/R, blade-spoke connection point (BSC) and TSR [47]. The latter was selected as the highest available in the simulation campaign. This procedure, already present in previous ALM tools from the authors [48], [49] is supposed to be more accurate than the ones used in the existing software, which are mainly based on an algebraic correction of the sampled AoA [50], [51].

3.1.2 Regularization kernel

As discussed earlier, to avoid non-physical discontinuities in the solution, the forces have to be projected into the CFD domain using a smearing function. In the current work, three variations of the Gaussian function have been considered:

1- Isotropic Gaussian [13], *iso*, where the forces are distributed equally in the chord and thickness directions in a cylindrical shape. This function reads:

$$\eta(r) = \frac{1}{\beta^2\pi} exp\left[-\left(\frac{|r|}{\beta}\right)^2\right] \tag{6}$$

2- Anisotropic Gaussian [32], *aniso*, where the forces are distributed in an elliptical shape using different kernel widths in chord and thickness directions; β_c and β_t, respectively. This function reads:

$$\eta(r_c,\, r_t) = \frac{1}{\beta_c\sqrt{\pi}} exp\left[-\left(\frac{|r_c|}{\beta_c}\right)^2\right] \cdot \frac{1}{\beta_t\sqrt{\pi}} exp\left[-\left(\frac{|r_t|}{\beta_t}\right)^2\right] \tag{7}$$

3- Anisotropic Gaussian-Gumbel [33], *GG*, which is similar to the anisotropic Gaussian. However, it has a Gumbel function applied to the chordwise direction that resembles the aerofoil physical shape. This function reads:

$$\eta(r_c,\, r_t) = \frac{1}{\beta_c} exp\left[-\left(\frac{|r_c|}{\beta_c}\right)\right] \cdot exp\left[-exp\left[-\left(\frac{|r_c|}{\beta_c}\right)\right]\right] \cdot \frac{1}{\beta_t\sqrt{\pi}} exp\left[-\left(\frac{|r_t|}{\beta_t}\right)^2\right] \tag{8}$$

In these functions, r is the distance between the generic cell centroid and the actuator line, and β is the kernel width parameter. In order to nondimensionalize β, it has been related in this work to the characteristic airfoil dimension, which in this case is the chord length, c [11]. An illustration of the kernel shapes that have been used in the present work is shown in Fig. 5.

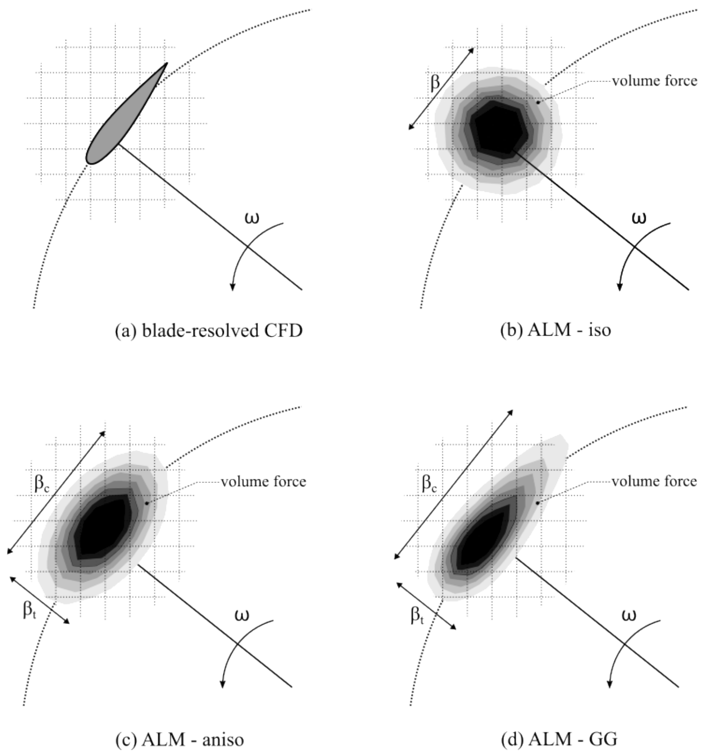

Figure 5 – (a) blade-resolved CFD illustration compared with the ALM kernel shapes employed in the present study (b) isotropic Gaussian, (c) anisotropic Gaussian, and (d) anisotropic Gaussian-Gumbel.

3.2 Frozen ALM

The *Frozen ALM* approach introduced by [31] has been considered in the present work as a starting point to further develop the concept as to apply it to the study of Darrieus turbines. In particular, this approach is useful as it enables the distinction between the errors due to the aerodynamic coefficients or dynamic stall model and those due to the insertion of forces in the domain. Basically, in the frozen ALM, the aerodynamic coefficients are not computed from the tabulated airfoil polar data, but are instead obtained directly from a blade-resolved CFD simulation. Hence, the uncertainties related to the quality of the polar data, dynamic stall model, and ad hoc correction models are removed.

The *Frozen ALM* was first used as a calibration method for the kernel widths, β_c, and β_t, using a static airfoil simulation. The calibration was conducted by obtaining a mean square error, E^2, between the flow field of the Frozen-ALM and the blade-resolved CFD, which gave an insight into the influence of the kernel width, thus allowing a wide range of interactions between different values of β_c and β_t. More in detail, E^2 was calculated between the blade-resolved CFD solution and that of the frozen ALM, as presented in Eq. (9):

$$E^2 = \frac{1}{A}\iint |{u_{ALM}}^2 - {u_{CFD}}^2| + |{v_{ALM}}^2 - {v_{CFD}}^2| dxdy \qquad (9)$$

where A is the domain area (except for the space allocated by the airfoil for the frozen ALM cases), u and v are the velocity components in X and Y directions, respectively. Figure 6 shows a schematic representation of the calibration technique workflow.

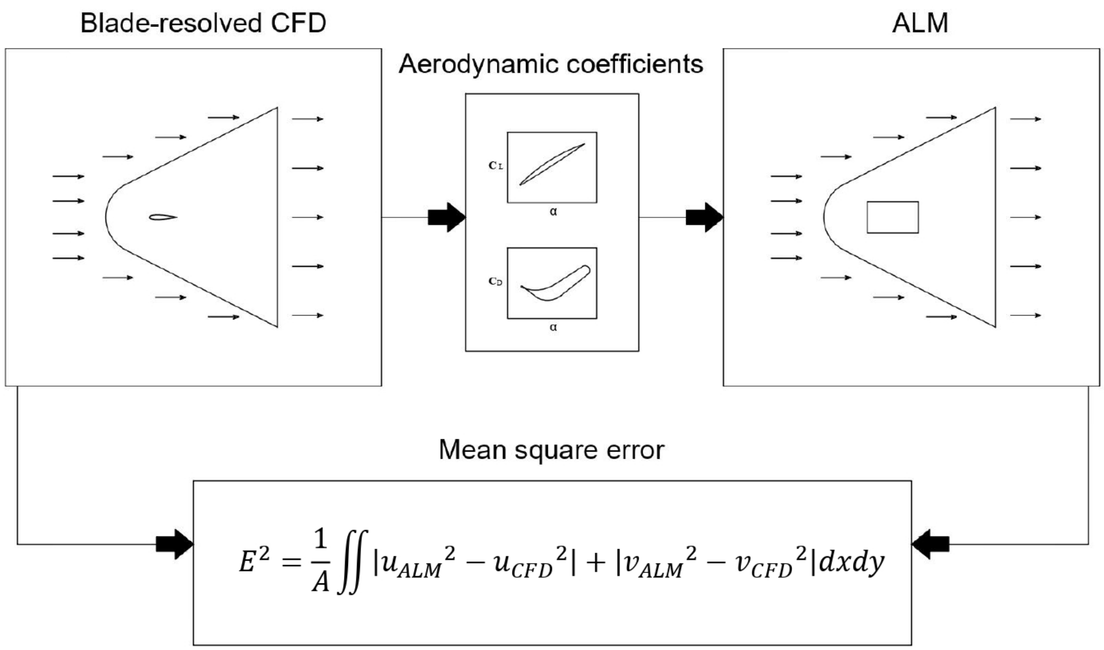

Figure 6 – Schematic representation of the kernel size calibration algorithm.

After calibrating the kernel width, the *Frozen ALM* was employed in a transient case of Darrieus turbine to assess the effect of the kernel shape in the context of a transient turbine case. In this case, the loads are extracted from a blade-resolved CFD case and then sent to the ALM code to be projected into the computational grid as equivalent volume momentum sources.

3.3 CFD set-up

3.1 Turbine model

All two-dimensional simulations were carried out with an unsteady Reynolds-Averaged Navier-Stokes (URANS) approach via the commercial solver ANSYS® FLUENT®, in the 2020 R2 release. For turbulence closure, the *k-ω* Shear Stress Transport (SST) model was selected [52]: compared to the other models available, it provides better accuracy and stability in unsteady flow conditions such as the ones experienced by VAWT blades, with massively separated flows and strong pressure gradients [10]. For detailed information about the settings for adopted numerical schemes, convergence definition, maximum inner iterations, and residuals, please refer to [10] and [53].

3.2 Domain and boundary conditions

An *open-field* domain was chosen for the analysis. The corresponding dimensions, parameterized with respect to turbine diameter D (see Fig. 7), were selected according to the sensitivity analysis from [48]. This allowed minimizing the disturbance induced by the turbine on the freestream flow, justifying the application of the standard *far field* boundary conditions commonly adopted for external flows. In detail, a uniform velocity, turbulent kinetic energy k, and length scale L were applied at the inlet based on the testing conditions of the considered test case. The turbulent quantities, in particular, were estimated according to the test inlet turbulent intensity and length scale. At the outlet, uniform atmospheric pressure was imposed, while for the other patches the *symmetry* condition was adopted.

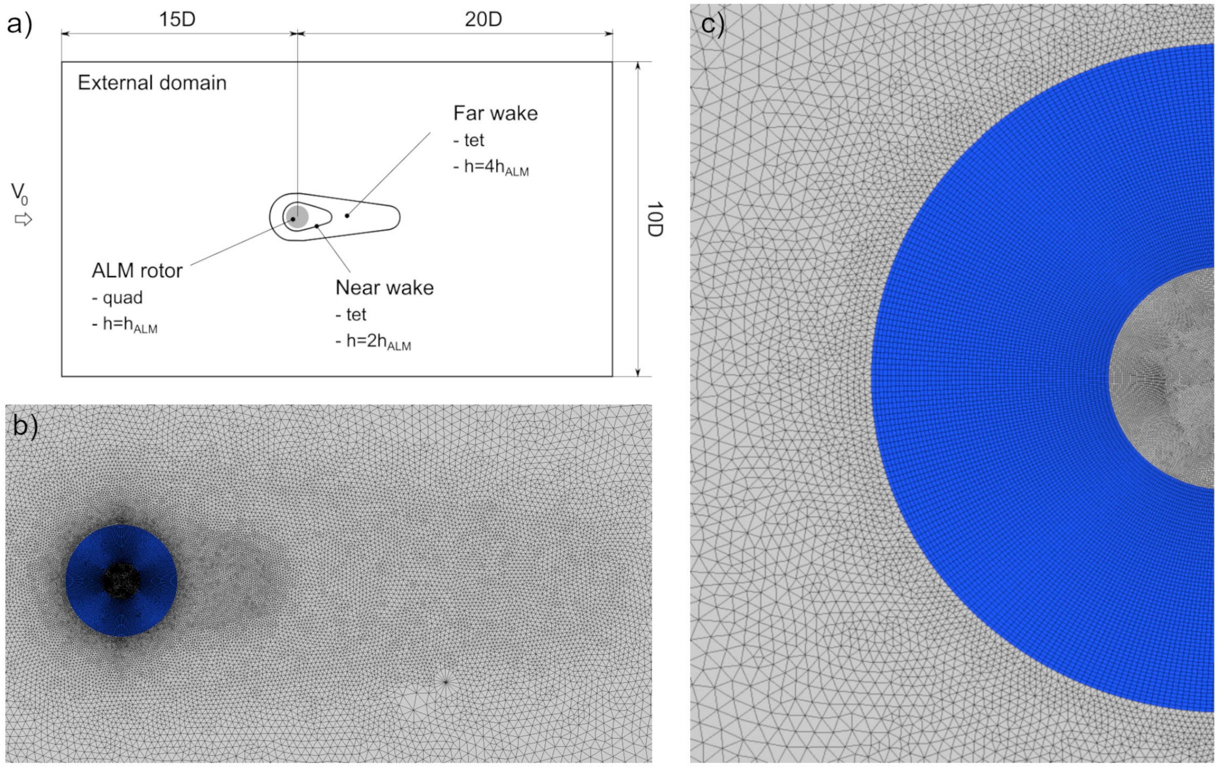

Figure 7 – a) details of the computational domain, b) overall grid, and c) ALM region grid.

3.3 Grid

The computational domain was discretized with a hybrid meshing strategy. As shown in Fig. 7, the CFD domain was divided into three separated fluid zones, according to the main features commonly found in a Darrieus turbine operating in an open-field environment:

- *Rotor ALM region:* The toroid encompassing the turbine rotor, where the forces are applied. In contrast with the rest of the domain, this region was discretized with a structured mesh, according to the requirements of the ALM. The number of elements in the azimuthal direction is directly proportional to the timestep used for the CFD simulations so that no discontinuity occurs when advancing the actuator line in the domain. The cell dimensions in the radial and spanwise direction, on the other hand, were chosen so that a cell Aspect Ratio as close as possible to 1 is achieved, at least on the turbine trajectory. This avoids the distortion of applied volume force distribution. The element size in this region is referred to in this paper as Δh and is always related to the kernel width β. A dedicated analysis of the model sensitivity to ALM region element size Δh is presented in Section 6.4;
- *Wake region:* An unstructured quad-dominant mesh was used for the drop-shaped refinement region near the rotor, which is necessary to properly capture the turbine blockage and wake development. As shown in Fig. 7, this region is divided into two separate zones: a *near*- and *far-wake* one. The former, characterized by a cell dimension h_{NW}, always taken as $2\Delta h$ comprehends the zone where the highest wake mixing is encountered. The latter, with

$h_{FW}=2h_{NW}$, serves to both resolve the far wake development and ensure a smooth transition from the rotor to the external domain;

- *External region:* The prismatic zone representing the external flow domain, discretized with tetrahedral elements.

4. Results

Initially, in Section 4.1, a calibration of the kernel width was conducted using the *Frozen ALM* approach, by comparing the flow field of a two-dimensional blade-resolved CFD for a static airfoil with that of the *Frozen ALM*. Indeed, investigating the interactions between different levels of kernel sizes (from β_c or β_t = 0.1c to β_c or β_t = 0.5c) provided an insight into its influence. Thereafter, to investigate the effect of the kernel shape and size in the light of the performance complexities of the Darrieus rotor, the *Frozen ALM* approach was applied to a rotor case in Section 4.2. Then, in Section 4.3, using the standard ALM, different kernel widths were evaluated. In Section 4.4, the solution sensitivity to the grid size was analyzed for each of the employed kernel functions. Finally, in Section 4.5, some comparative analyses and remarks were highlighted.

An important aspect of this study is that two different rotors of different solidities were studied: *R1000*, which is a Darrieus Hydrokinetic Turbine (HKT), and *R500*, which is a Darrieus Vertical Axis Wind Turbine (VAWT). Using such an approach was useful in understanding the significance of the results in the context of different fluids and turbine geometries.

4.1 Static airfoil: kernel calibration

To investigate the influence of the kernel width, a parametric study has been first carried out using different combinations of β_c and β_t values. To do so, the frozen ALM approach was utilized for a static NACA0018 airfoil case at AoA = 15°, for which the blade-resolved CFD simulation was showing the presence of flow separation. The blade forces resulting from the latter simulation were then projected into the CFD flow field using different smearing functions as discussed in Section 3.2.

Figure 8 shows the contours of the normalized square error E^2/E^2_{min} for different values of β_c and β_t, where E^2_{min} is the minimum normalized square error obtained; the isotropic line is shown in Fig. 8-a. Overall, the results show that the solution is more sensitive to the kernel width in the chord direction β_c than to the thickness direction β_t. This observation agrees with the theoretical analysis conducted by Martínez-Tossas et al. [31]. Furthermore, the results show that, generally, the size of the kernel has a larger impact in the case of the *GG* compared to the *aniso*. From these results, it could be observed that using a kernel width in the thickness-wise direction β_t as half of that in the chord-wise direction β_c would be the best practice, especially while using a large value of β_c, e.g., β_c > 0.3c. The latter remark could be even more noticeable in the *GG* case as shown in Fig. 8-b.

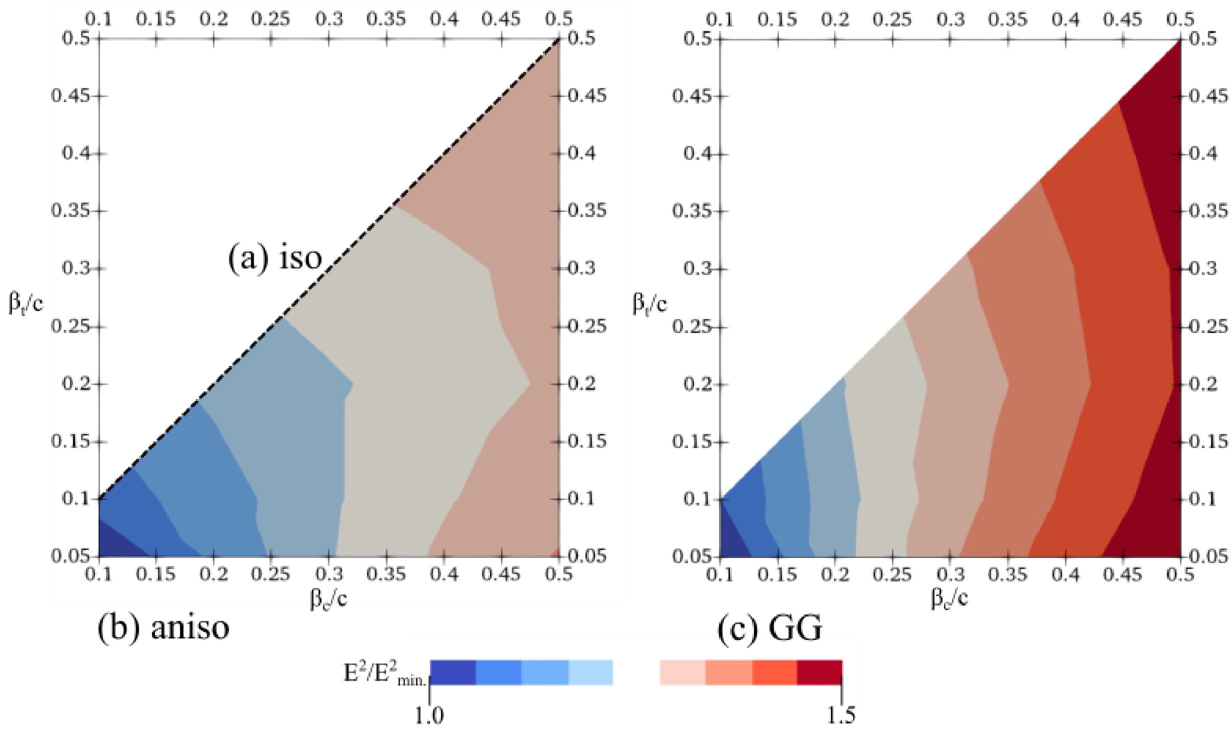

Figure 8 – Contours of the nominal mean square error E^2/E^2_{min} of the velocity field for (a) anisotropic Gaussian and (b) anisotropic Gaussian-Gumbel obtained for different kernel widths, β_c and β_t.

4.2 Rotor simulations: effect of kernel shape

To study the effect of the kernel shape, the *FrozenALM* has been employed for the *R500* and the *R1000* models in order to eliminate the uncertainties related to polar data. Figure 9 shows the sampled angle of attack for *FrozenALM - iso*, *FrozenALM - aniso*, and *FrozenALM - GG* compared to that sampled from a blade-resolved CFD. It is important to point out here that the local velocity sampling for the blade-resolved CFD was conducted using the same *LineAverage* technique adopted for the ALM with the settings mentioned in Section 3.1. In the present cases of *FrozenALM*, kernel widths were taken as β_c = 0.1c and β_t = 0.05c for both the *aniso* and *GG* cases, while for the *iso* case, β = 0.1c has been used. As it can be seen, all frozen ALM cases - regardless of the employed smearing function - were able to sample the *AoA* around the hypothetical blade almost equally, which matches as well with the *AoA* sampled from the blade-resolved CFD.

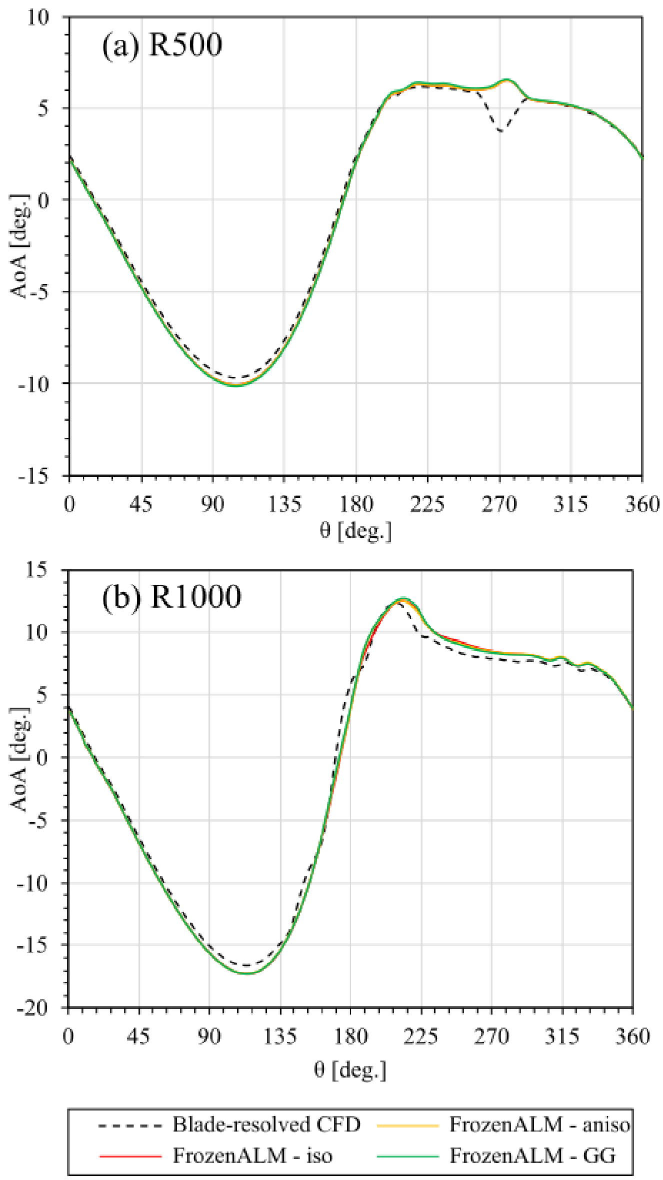

Figure 9 – Angle of attack sampling for the (a) R500 and (b) R1000 using FrozenALM of different smearing functions: iso, aniso, and GG compared to that sampled from the blade-resolved CFD.

Figure 10 shows the contours of the dimensionless velocity V/V_∞ for the *R1000* case at different azimuth positions, θ, for the blade-resolved CFD compared to that of the *FrozenALM* solutions. Although the three kernel functions showed the same AoA predictions (see Fig. 9), the blade wakes resulting from the *FrozenALM-iso* seem to be more poorly represented compared to that of the *FrozenALM-aniso* and *FrozenALM-GG*, especially in the upstream azimuthal positions, e.g., θ = 60°, 120°, and 180°. The latter observation could be attributed to the narrow distribution of forces in the thickness direction for the anisotropic functions. On the other hand, the near wake of the rotor seems to be the same for all the smearing functions and matches with the blade-resolved CFD flow field.

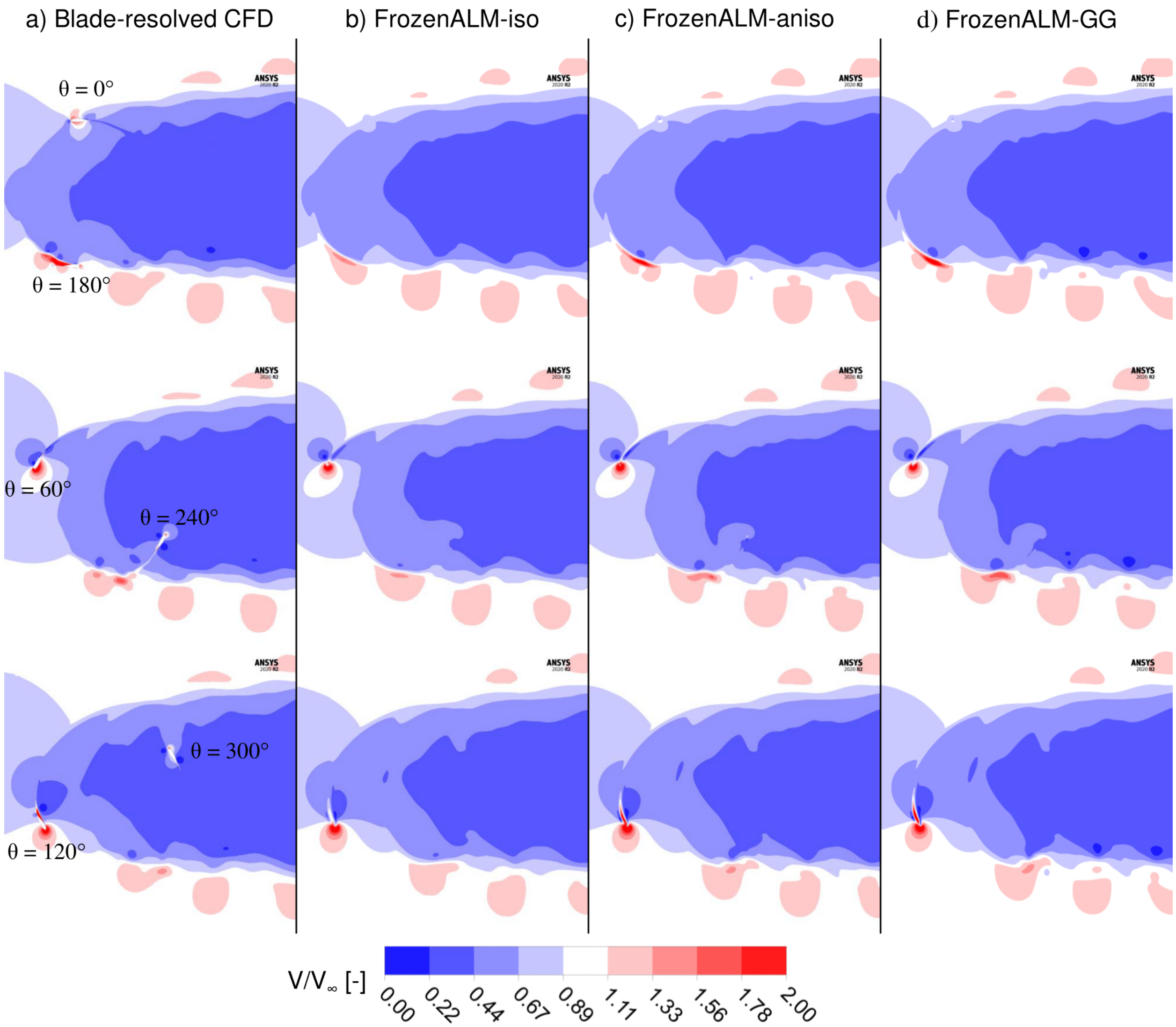

Figure 10 – Dimensionless velocity contours of *R1000* rotor at various blade azimuth positions for the blade-resolved CFD compared with frozen ALM cases using *iso*, *aniso*, and *GG* smearing functions.

4.3 Rotor simulations: effect of the kernel size

To investigate the effect of the kernel width in a transient context, a sensitivity analysis has been conducted for each of the three smearing functions. For both *aniso* and *GG*, the kernel width in the thickness-wise direction was always taken as $\beta_t = 2\beta_c$ as discussed earlier in Section 4.1. Regarding the grid size, the ALM grid element size was taken as $\Delta h = \beta_t/2$ for both *aniso* and *GG*, and $\Delta h = \beta/2$ for the *iso*.

4.3.2 R500 Rotor

Regarding the R500 VAWT rotor, Fig. 11 shows the prediction of the blade normal force coefficient C_N ($C_N = F_N/0.5\rho V_\infty^2$) and tangential force coefficient C_T ($C_T = F_T/0.5\rho V_\infty^2$) for multiple kernel widths for *ALM-iso* compared to that of the blade-resolved CFD and experimental results from [37]. As discussed, since a TSR of 4.5 is investigated here, the impact of dynamic stall is here negligible. Upon examination of the figure it is apparent that, compared to the blade-resolved CFD, the ALM was able to predict the blade's normal load during the upwind section regardless of the adopted kernel size. It must be noted that experimental data are subject to a high degree of uncertainty due to issues in the extrapolation of forces from PIV data [37]. In the downwind region, the ALM is slightly overpredicting the load. Figure 12 shows the normal force coefficient for *ALM-aniso* using various kernel widths and compared to that of blade-resolved CFD. Considerations similar to the above can be made here, where increasing the kernel width does not significantly influence the prediction of the load. Moving to the *ALM-GG*, Fig. 13 shows that, unlike the other two smearing functions, the Gumbel function seems to be more sensitive to the width of the kernel as observed earlier in Section 4.1. Adopting larger kernel widths leads to an overprediction in the load during the upwind region at 45° < θ < 70° and during the downwind region at 180° < θ < 315°.

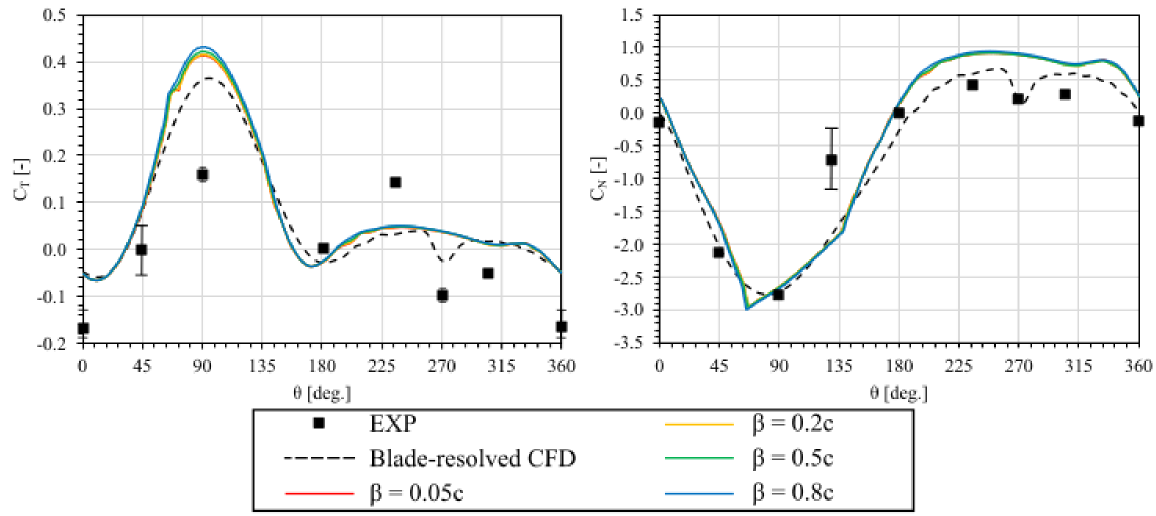

Figure 11 – **Predicted variation of tangential and normal forces coefficients for a single blade of R500 over a full revolution for the blade-resolved CFD and ALM-iso using different kernel widths compared with experimental data.**

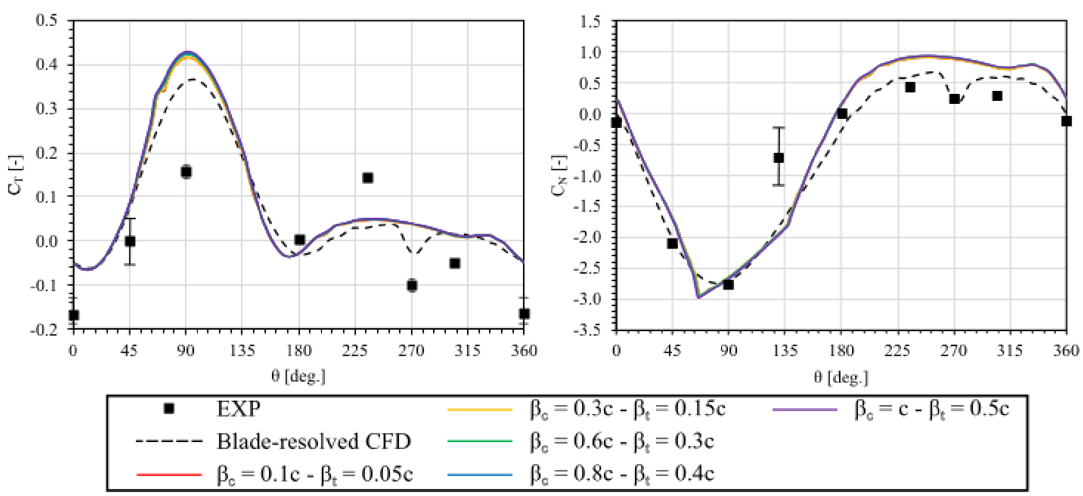

Figure 12 – **Predicted variation of tangential and normal forces coefficients for a single blade of R500 over a full revolution for the blade-resolved CFD and ALM-aniso using different kernel widths compared with experimental data.**

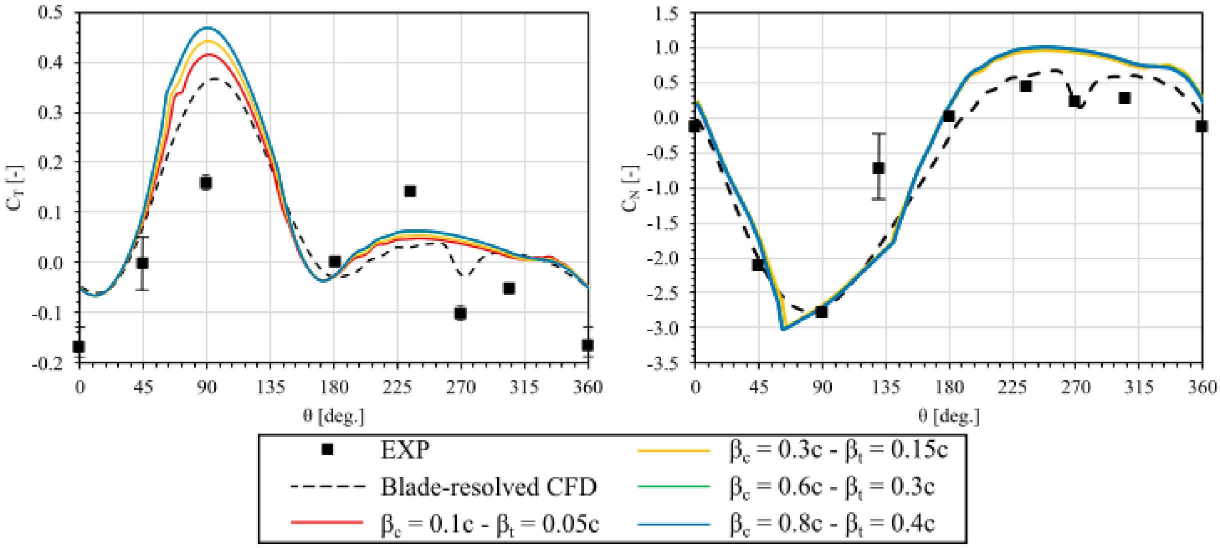

Figure 13 – Predicted variation of tangential and normal forces coefficients for a single blade of R500 over a full revolution for the blade-resolved CFD and ALM-GG using different kernel widths compared with experimental data.

4.3.2 R1000

Figure 14 shows the computed *R1000* blade normal and tangential coefficients over a full revolution for *ALM-iso* using different kernel widths compared to those of blade-resolved CFD. Overall, it can be noticed that the kernel width does not significantly affect the load predictions. More in detail, looking at the first quadrant of the blade azimuthal path (0° < θ < 90°), all kernel widths predicted the force similarly until reaching $\theta \approx 60°$, which corresponds to *AoA* = 10° (see Fig. 9), where the higher kernel widths result in a slight overestimation of the load. Thereafter, during the second azimuthal quadrant (90° < θ < 180°), the load predictions are perfectly matched for all cases. However, during the downstream azimuth positions (180° < θ < 360°), one can notice slight differences between the load estimation, which can be ascribed to the effect of velocity sampling within the shed vortex flow field. Generally, the vortical flow structure that is formed in the wake of the hypothetical blade during the upstream azimuthal path is convected downstream and interacts with blades during their downstream azimuthal path. The size and the intensity of those vortices are highly dependent on the adopted grid element size that is in turn a function of the kernel size. A detailed analysis is conducted for the flow field of ALM with different grid sizes and kernel shapes in Section 4.5.

Figure 15 shows the computed normal and tangential coefficients for the *R1000* using *ALM-aniso* with different kernel widths. From a perusal of the figure, one can note that the results are quite similar to those obtained from the *ALM-iso*, showing no significant effect of changing the kernel width. Moving to the *ALM-GG*, Fig. 16 reports the estimated normal and tangential force coefficients using different kernel sizes for the *R1000*. It can be observed that this smearing function is much more sensitive to the kernel size compared to the other circular and parabolic functions. The results of the *ALM-GG* show that differences in the load estimation start during the first quadrant and reach their maximum at $\theta \approx 75°$, where the load peaks. However, within the azimuthal range 100° < θ < 190°, the load predictions are almost the same for all the kernel widths. After that, and during almost the whole downstream azimuthal path (190° < θ < 360°), the loads are significantly different, especially at $\beta_c > 0.2c$. where the trend is that the larger the kernel size, the larger the force estimation. This was expected considering the sensitivity of the additional Gumbel function to the width of the kernel as discussed in Section 4.1.

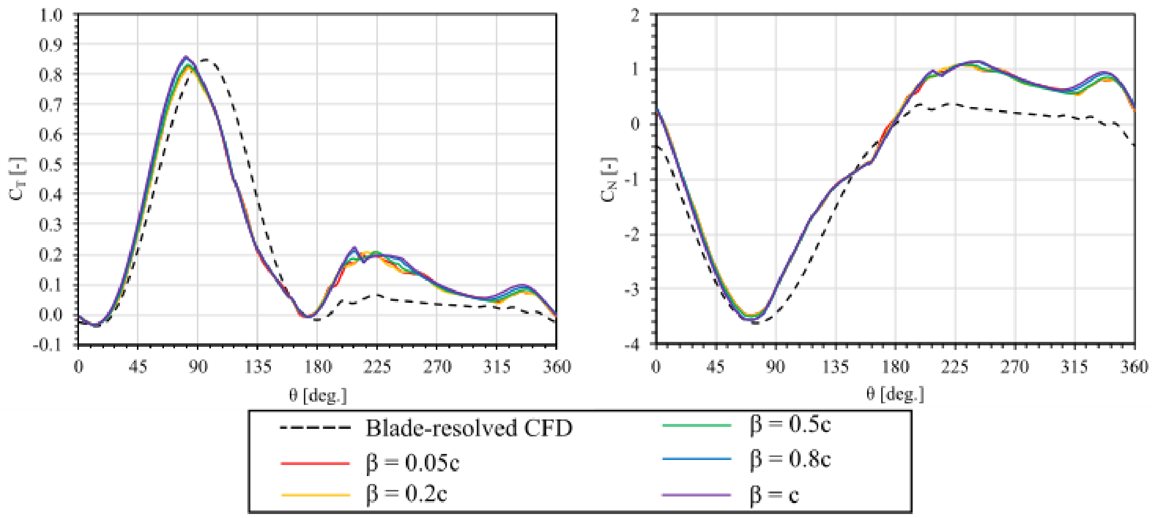

Figure 14 – Predicted tangential force variation for a single blade of R1000 over a full revolution for the blade-resolved CFD and ALM-iso using different kernel widths compared with experimental data.

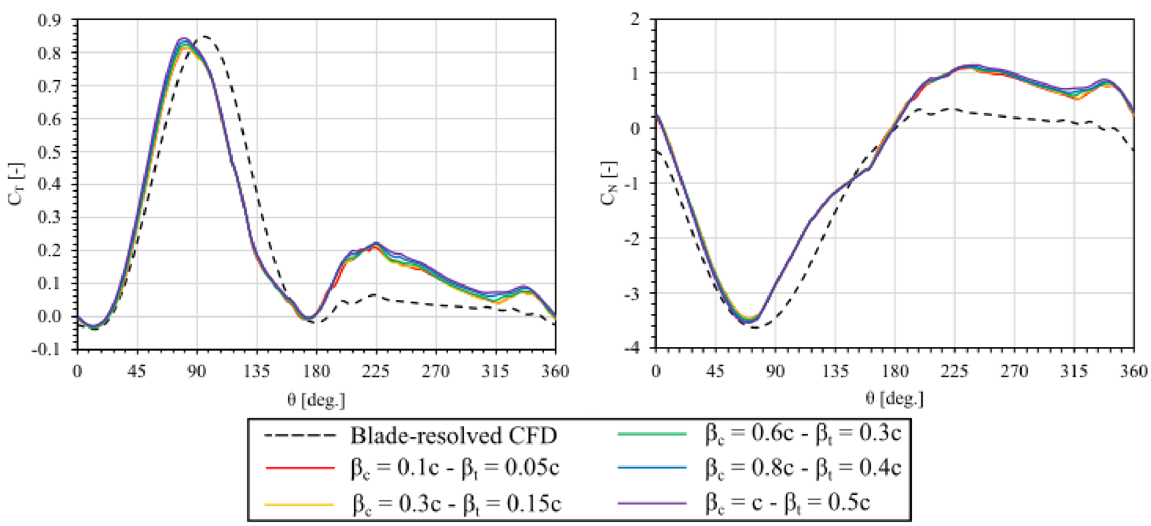

Figure 15 – Predicted tangential force variation for a single blade over a full revolution for the blade-resolved CFD compared with ALM-aniso using different kernel widths.

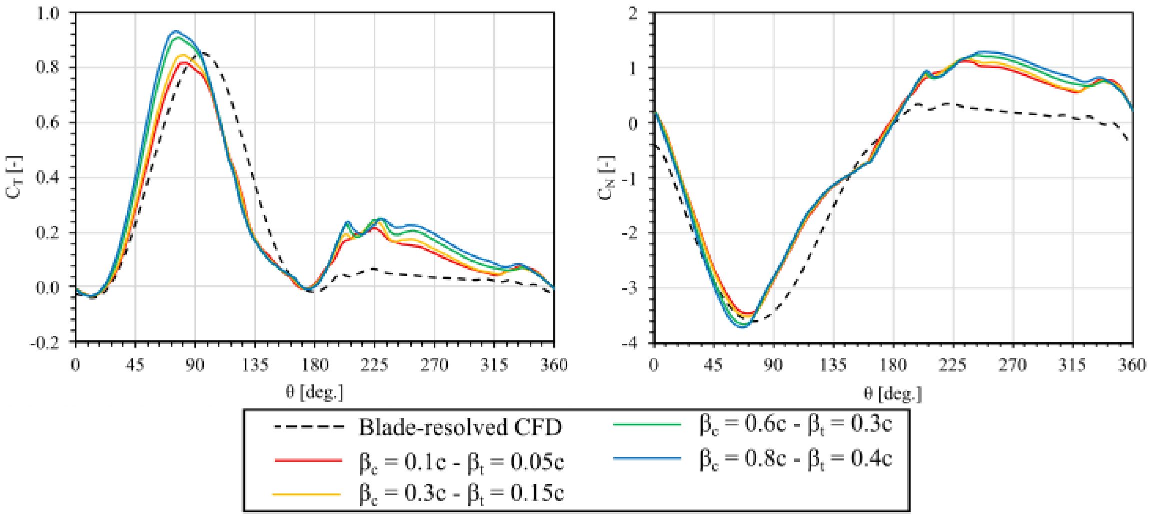

Figure 16 – Predicted tangential force variation for a single blade over a full revolution for the blade-resolved CFD compared with ALM-GG using different kernel widths.

4.4 Effect of grid size

To investigate the influence of ALM grid size Δh for each of the kernel shapes, a dedicated grid sensitivity analysis has been conducted for the *R1000*. Table 3 reports the details of the investigated set-ups. It is common practice in ALM to relate Δh with the size of the kernel β [13]. Based on previous literature on HAWTs, it is known that a ratio of $\Delta h = \beta/2$ would guarantee a stable and robust solution. In the present analysis, the question was which kernel width should be related to the grid size while using non-isotropic functions, e.g., β_c or β_t. Thus, several models were tested using the same kernel width while varying the size of the grid element size. For *ALM-iso*, $\beta = 0.5$c has been used, and for *ALM-aniso* and *ALM-GG*, $\beta_c = 0.6$c - $\beta_t = 0.3$c and $\beta_c = 0.2$c - $\beta_t = 0.1$c, respectively.

Figure 17 shows the results of the normal force for the three evaluated kernel shapes using different grid sizes. It can be seen that for the *ALM-iso*, using $\Delta h = \beta/2$ and $\Delta h = \beta/1.5$ produces the same normal force profiles, while when increasing Δh so as to be the same size of the kernel, one can notice the instability of the predicted force profile at the positions where flow separation is expected, e.g., $60° < \theta < 90°$ and $240° < \theta < 300°$.

For *ALM-aniso*, the ALM element size Δh has been related first to the kernel in the thickness direction β_t, and as can be seen from Fig. 18, the performance prediction results seem to be unaffected by the grid size until Δh reaches 1.5 β_t, where the instabilities in the normal force profile start to appear and it increases significantly at $\Delta h = 2\beta_t$, which corresponds in this case to $\Delta h = \beta_c$. On the other hand, for *ALM-GG*, the load predictions seem to be more sensitive to the mesh size, as seeable from Fig 19, at $\Delta h = \beta_t$, instabilities in the load predictions could be seen clearly at $75° < \theta < 100°$ and $200° < \theta < 330°$.

Table 3 – Grid senestivity analysis set-ups.

Set-up		*Δh [mm]*	Number of elements
iso - β = 0.5c	$\Delta h = \beta/2$	62.5	11860
	$\Delta h = \beta/1.5$	83.3	10763
	$\Delta h = \beta$	125	9854
aniso - β_c = 0.6c, β_t = 0.3c	$\Delta h = \beta_t/2$	37.5	16764
	$\Delta h = \beta_t/1.5$	50	13392
	$\Delta h = \beta_t$	75	11017
	$\Delta h = 1.5\beta_t$	112.5	9991
	$\Delta h = 2\beta_t$	150	9559
GG - β_c = 0.2c, β_t = 0.1c	$\Delta h = \beta_t/2$	12.5	72819
	$\Delta h = \beta_t/1.5$	16.7	44655
	$\Delta h = \beta_t$	25	25086

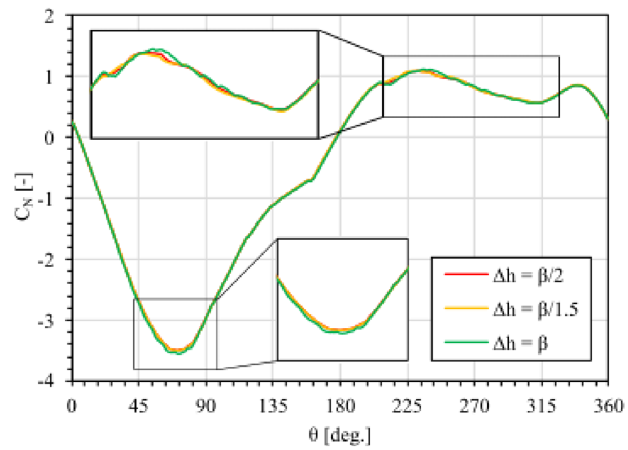

Figure 17 – Variation of the predicted normal force coefficient of *R1000* for the ALM-iso (β = 0.5c) using different grid sizes.

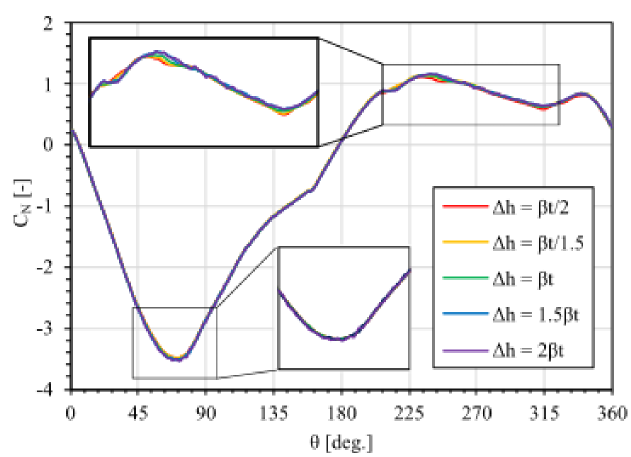

Figure 18 – Variation of the predicted normal force coefficient of *R1000* for the ALM-aniso (β_c = 0.6c - β_t = 0.3c) using different grid sizes.

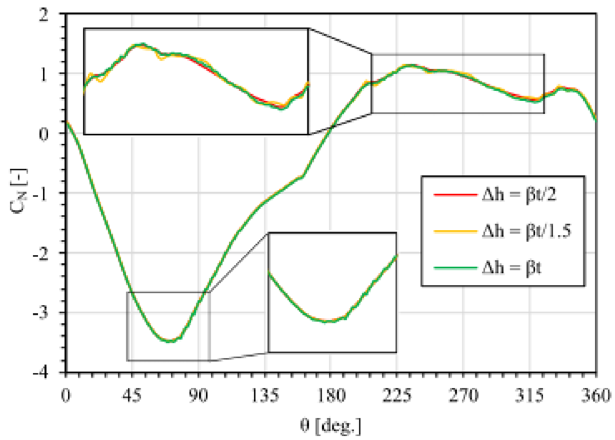

Figure 19 – Variation of the predicted normal force coefficient of *R1000* for the ALM-GG (β_c = 0.2c - β_t = 0.1c) using different grid sizes.

4.5 Comparative analyses and additional remarks

Figure 20 shows the resulting hysteresis loops of lift coefficient, C_L, for the three variations of the ALM using kernel functions of *iso*, *aniso*, and *GG*, compared to those obtained from the *FrozenALM*, which are basically the same as those of the blade-resolved CFD. As can be seen in Fig 20-a for *R500*, one can observe that the kernel shape does not affect the prediction of C_L, and all the ALM variations show the exact same C_L, which almost matches that of the *FrozenALM*. However, the ALM was not able to reproduce the unsteady effects which can be noticed around AoA ≈ 5° for the lift coefficient of the *FrozenALM*. Moving to *R1000* in Fig. 20-b, significant deviations could be noticed between the C_L of the *FrozenALM* and that obtained from the standard ALM variations. Also, it shows that the kernel shape does not influence the C_L predictions, despite the slight differences that could be noticed at high angles of attack, e.g., AoA < -10°, which are attributed to the implementation of the dynamic stall model inside the code. Generally, comparing the C_L results of the *FrozenALM* with that of the standard ALM shows that the presence of the dynamic stall phenomenon plays the most important role in producing a reliable and accurate load prediction.

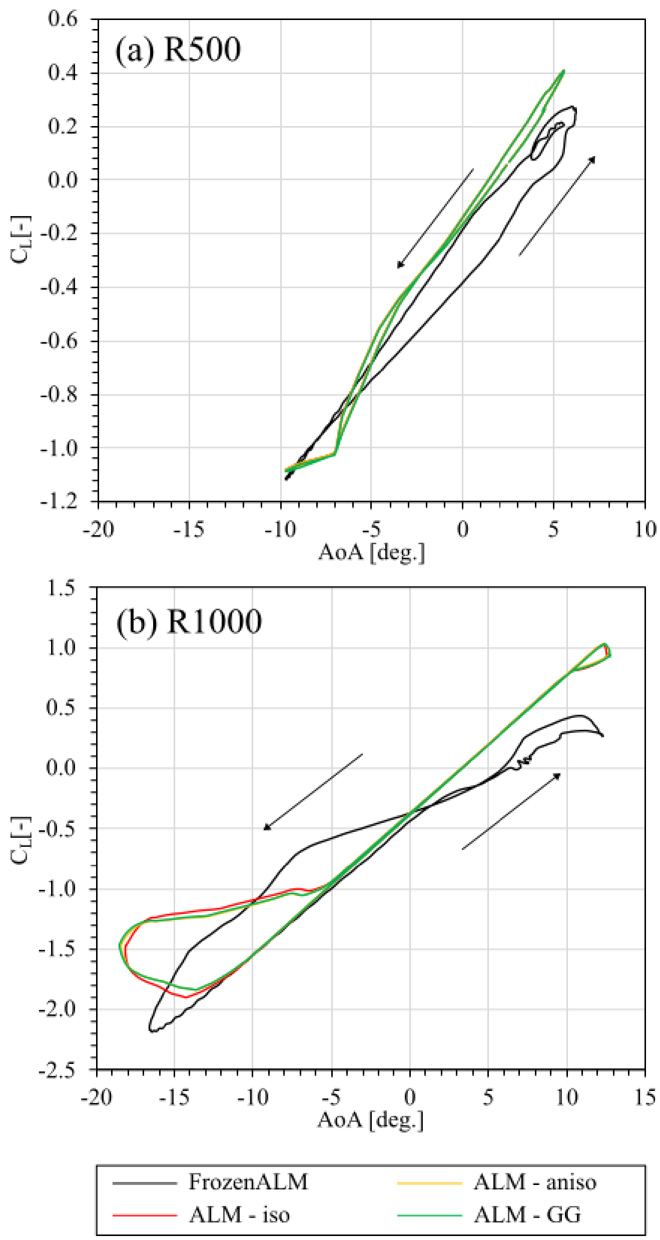

5.

Figure 20 – Hysteresis loop of lift coefficients obtained from *FrozenALM* compared to that of the ALM variations using different kernel shapes.

Figure 21 shows the contours of dimensionless vorticity of *R1000* for different ALM cases with different kernel shapes, widths, and grid sizes compared to that of the blade-resolved CFD. From Figs. 21-b and 21-d, it can be noticed that the flow field of the *ALM-aniso* is extremely sensitive to the width of the kernel, despite that both cases resulted in the same load predictions (see Fig. 15). Moreover, comparing the latter cases to the blade-resolved CFD presented in Fig. 21-a, and focusing on the shear layers that define the wake borders, one can observe that the *ALM-aniso* with the smallest kernel width (β_c = 0.1c – β_t = 0.05c) reproduced the diffusion of the red anticlockwise vortices more accurate compared to that with the larger kernel width (β_c = 0.6c – β_t = 0.3c).

However, the blue clockwise vortices tend to be more compact in the case of the smaller kernel width compared to that of the blade-resolved CFD. Conversely, the larger kernel width reproduced the convection of these vortices more similar to that of the blade-resolved CFD.

Moving to the *ALM-iso*, Fig. 21-e and 21-f bring to the same conclusion that has been observed for the *ALM-aniso*: despite using β = 0.05c and β = 0.5c showed the same load predictions (see Fig. 14), the flow fields of both cases are completely different, showing more compact vortices in the wake region in the case of smaller kernel width. The latter observation is attributed more to the grid size than to either the kernel shape or size. To elaborate on that, one can compare the cases in Fig. 21-c and 21-d or in Fig. 21-b and 21-f. The former shows the *ALM-aniso* of the same kernel widths (β_c = 0.6c – β_t = 0.3c) but with different grid element sizes in the ALM region (Δh), while the latter shows the ALM results of the same grid size but employing two different kernel shapes, *iso* and *aniso*. Interestingly, the ALM is able to reproduce the wake flow field similarly for both *ALM-iso* and *ALM-aniso* if the same grid element size is used. Whereas, in the case of employing the same kernel shape, but with a different grid element size, the flow field in the wake is significantly different.

From the latter analysis, one can say that the effect of the shape of the kernel is not significant in either the load prediction or the flow field; conversely, it can be said that the grid size plays the most important role in reproducing the flow field wake.

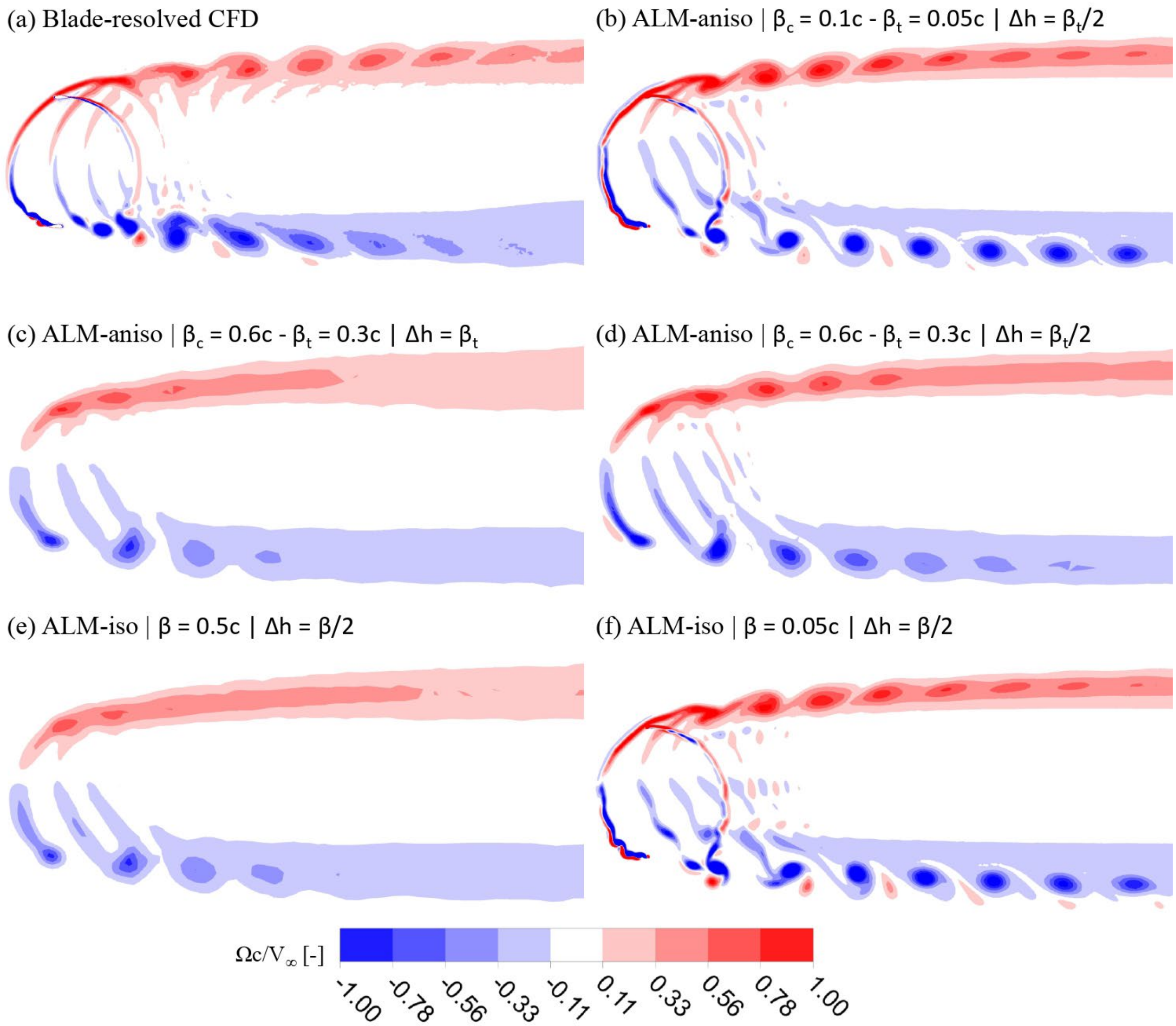

Figure 21 – Dimensionless vorticity contours of *R1000* for various ALM cases using different kernel shapes, sizes, and grid sizes compared to that of the blade-resolved CFD.

5. Discussion

While the amount of results showed in Section 4 can make the reader lose the narrative path, the information resulting from a general interpretation of them is quite clear and of capital relevance in the field of Darrieus VAWT simulation.

Overall, the comparison with both experiments and blade-resolved CFD showed that the current implementation of the ALM [23] is adequate to predict both rotor performance and flow field with an acceptable level of accuracy at medium and high tip-speed ratios, provided that the correct aerodynamic data is fed into the code, and the grid is fine enough to capture the complexities of the wake flow structures.

The shape of the kernel, which has been long deemed to represent a major source of discrepancies [23] seems not to be relevant in the case of Darrieus vertical axis turbines. This differs from the ALM for HAWTs, where previous works have demonstrated the role of non-isotropic kernel shapes in reproducing the wake more accurately [28] [29] [30]. In VAWTs the effect of the kernel size on the other hand, which has been deemed a source of discrepancies in reproducing the shed vortical structures of the Darrieus turbine wake [18], seems to be mutually dependent on the grid size but does not itself affect the accuracy of the solution, except in the case of employing *GG* kernel function. As remarked in Fig. 21, using *aniso* kernel shape with a relatively large kernel size, e.g., β_c = 0.6c and β_t = 0.3c, and with a proper grid refinement, can reproduce the wake flow field with good accuracy compared to blade-resolved CFD. Indeed, it is important to note that the sampling strategy for the blade local flow field plays a crucial role in minimizing the influence of the kernel shape or size on the ALM solution. For example, the conventional ALM sampling method which has been implemented either in the original work of Sørensen and Shen [11] or in most of the works that follow, is based on sampling the velocity directly along the actuator line itself, in another word, at the center of the bound vortex, where the blade local flow effects are not seen. The latter method could be sensitive to the kernel size as noted by Martínez et al. [54]. However, the *LineAverage* strategy, employed in this work, does not have this limitation, since the local velocity is sampled as an integral average along a closed line around the actuator line.

Moving toward the influence of the aerodynamic coefficients data, it has been demonstrated that the ALM is capable of generating an extremely accurate wake flow field, close to that of the blade-resolved CFD (see Fig. 10) if the code is fed with the correct polar data. The *FrozenALM* solution showed that the aerodynamic coefficients play the most important role in the ALM solution accuracy. In particular, in the case of the *R1000* at TSR = 2.5, where dynamic stall plays an important role, the lift coefficient results showed there are significant deviations between the lift estimated by the ALM code and that used for the *FrozenALM* case. Accordingly, a better dynamic stall model is indeed the real key factor that could lead to an improvement of the ALM accuracy.

6. Conclusions

The present work showed a dedicated assessment of the role of the *input polar data*, *dynamic stall model*, and the *force smearing function* in ALM in the context of the Darrieus rotor.

To separate the effects, the *FrozenALM* approach was developed, and implemented for the first time on Darrieus turbines. This is based on feeding the ALM with aerodynamic forces extracted directly from blade-resolved CFD, which allowed evaluating the impact of the kernel shape, while blocking the influence of polar data quality and dynamic stall modelling. To support the analyses, two rotors were analyzed, i.e., the *R500*, a VAWT with a low solidity of 0.12 operating at stable conditions at TSR of 4.5, and the *R1000*, a HKT with a medium solidity of 0.25 operating at its optimum TSR of 2.5. The results of the *FrozenALM* showed that the kernel shape does not significantly influence the capabilities of the ALM to either predict the blade loads or to reproduce the wake flow field. Rather, it showed that, the ALM is able to generate extremely accurate solutions of the flow field, almost equivalent to blade-resolved CFD, if the aerodynamic forces are provided correctly.

Using the standard ALM, three different kernel functions have been tested in different sizes: (a) *iso* which distributes the forces in a circular shape, (b) *aniso* which has a parabolic shape, and (c) *GG* which also takes a parabolic shape but with a Gumbel function in the chordwise direction, making the distribution closer to that of the airfoil. It has been concluded that the size of the kernel does not significantly affect the solution, except in the case of using *GG* function, where the additional Gumbel function is very sensitive to the width of the kernel. Thereafter, an assessment of the grid size influence has been conducted for the three kernel shapes, showing that, regardless of the kernel shape and size, the grid resolution is the key factor that significantly influences the quality of reproducing the flow field. Further, the grid sensitivity analysis showed that using ALM grid size, $\Delta h = \beta/2$ is a best practice while using *iso* kernel, and $\Delta h = \beta_t/2$ while using *aniso* or *GG* kernels.

Finally, the analysis of the two rotors under two different operating conditions allowed evaluating the role of the dynamic stall model in the accuracy of the ALM. The ALM load estimation for the *R500* (no dynamic stall) was much closer to the blade-resolved CFD compared to that of the *R1000* (dynamic stall massively present). Upon comparing the aerodynamic coefficients from the *FrozenALM* and the standard ALM, it has been concluded that the cases of large dynamic stall presence resulted in a significant mismatch in the lift coefficient data compared to those derived from blade-resolved CFD. Thus, a better dynamic stall model is indeed the real key factor that could lead to an improvement in the ALM accuracy. To this end, further research will be devoted at developing a dynamic stall model that could account for the special characteristics of Darrieus rotors. This would make the ALM more reliable, especially in dealing with advanced applications such as floating offshore, multiple rotors, and urban applications.

References

[1] P. F. Melani, F. Balduzzi, G. Ferrara, and A. Bianchini, 'How to extract the angle attack on airfoils in cycloidal motion from a flow field solved with computational fluid dynamics? Development and verification of a robust computational procedure', *Energy Convers. Manag.*, vol. 223, p. 113284, Nov. 2020, doi: 10.1016/j.enconman.2020.113284.

[2] O. S. Mohamed, A. M. R. Elbaz, and A. Bianchini, 'A better insight on physics involved in the self-starting of a straight-blade Darrieus wind turbine by means of two-dimensional Computational Fluid Dynamics', *J. Wind Eng. Ind. Aerodyn.*, vol. 218, p. 104793, Nov. 2021, doi: 10.1016/j.jweia.2021.104793.

[3] O. S. Mohamed, A. Ibrahim, and A. M. R. El Baz, 'CFD Investigation of the Multiple Rotors Darrieus Type Turbine Performance', presented at the ASME Turbo Expo 2019: Turbomachinery Technical Conference and Exposition, Nov. 2019. doi: 10.1115/GT2019-91491.

[4] U. S. Paulsen, H. A. Madsen, J. H. Hattel, I. Baran, and P. H. Nielsen, 'Design Optimization of a 5 MW Floating Offshore Vertical-axis Wind Turbine', *Energy Procedia*, vol. 35, pp. 22–32, Jan. 2013, doi: 10.1016/j.egypro.2013.07.155.

[5] F. Balduzzi, A. Bianchini, E. A. Carnevale, L. Ferrari, and S. Magnani, 'Feasibility analysis of a Darrieus vertical-axis wind turbine installation in the rooftop of a building', *Appl. Energy*, vol. 97, pp. 921–929, Sep. 2012, doi: 10.1016/j.apenergy.2011.12.008.

[6] F. Balduzzi, P. F. Melani, G. Soraperra, A. Brighenti, L. Battisti, and A. Bianchini, 'Some design guidelines to adapt a Darrieus vertical axis turbine for use in hydrokinetic applications', *E3S Web Conf.*, vol. 312, p. 08017, 2021, doi: 10.1051/e3sconf/202131208017.

[7] C. J. S. Ferreira, H. Bijl, G. van Bussel, and G. van Kuik, 'Simulating Dynamic Stall in a 2D VAWT: Modeling strategy, verification and validation with Particle Image Velocimetry data', *J. Phys. Conf. Ser.*, vol. 75, p. 012023, Jul. 2007, doi: 10.1088/1742-6596/75/1/012023.

[8] M. Raciti Castelli, A. Englaro, and E. Benini, ‘The Darrieus wind turbine: Proposal for a new performance prediction model based on CFD’, *Energy*, vol. 36, no. 8, pp. 4919–4934, Aug. 2011, doi: 10.1016/j.energy.2011.05.036.
[9] A. Bianchini, F. Balduzzi, G. Ferrara, G. Persico, V. Dossena, and L. Ferrari, ‘A Critical Analysis on Low-Order Simulation Models for Darrieus Vawts: How Much Do They Pertain to the Real Flow?’, *J. Eng. Gas Turbines Power*, vol. 141, no. 1, Sep. 2018, doi: 10.1115/1.4040851.
[10] F. Balduzzi, A. Bianchini, R. Maleci, G. Ferrara, and L. Ferrari, ‘Critical issues in the CFD simulation of Darrieus wind turbines’, *Renew. Energy*, vol. 85, pp. 419–435, 2016, doi: 10.1016/j.renene.2015.06.048.
[11] J. N. Sørensen and W. Z. Shen, ‘Numerical Modeling of Wind Turbine Wakes’, *J. Fluids Eng.*, vol. 124, no. 2, pp. 393–399, May 2002, doi: 10.1115/1.1471361.
[12] W. Z. Shen, J. N. Sørensen, and R. Mikkelsen, ‘Tip Loss Correction for Actuator/Navier–Stokes Computations’, *J. Sol. Energy Eng.*, vol. 127, no. 2, pp. 209–213, Apr. 2005, doi: 10.1115/1.1850488.
[13] M. Shives and C. Crawford, ‘Mesh and load distribution requirements for actuator line CFD simulations’, *Wind Energy*, vol. 16, no. 8, pp. 1183–1196, 2013, doi: 10.1002/we.1546.
[14] N. Troldborg, J. N. Sorensen, and R. Mikkelsen, ‘Numerical simulations of wake characteristics of a wind turbine in uniform inflow’, *Wind Energy*, vol. 13, no. 1, pp. 86–99, 2010, doi: 10.1002/we.345.
[15] ‘Large-eddy simulation of a very large wind farm in a stable atmospheric boundary layer: Physics of Fluids: Vol 23, No 6’. https://aip.scitation.org/doi/10.1063/1.3589857 (accessed May 23, 2022).
[16] S. Shamsoddin and F. Porté-Agel, ‘Large Eddy Simulation of Vertical Axis Wind Turbine Wakes’, *Energies*, vol. 7, no. 2, Art. no. 2, Feb. 2014, doi: 10.3390/en7020890.
[17] P. Bachant, A. Goude, and M. Wosnik, ‘Actuator line modeling of vertical-axis turbines’, arXiv, arXiv:1605.01449, Sep. 2018. doi: 10.48550/arXiv.1605.01449.
[18] V. Mendoza, P. Bachant, C. Ferreira, and A. Goude, ‘Near-wake flow simulation of a vertical axis turbine using an actuator line model’, *Wind Energy*, vol. 22, no. 2, pp. 171–188, 2019, doi: 10.1002/we.2277.
[19] R. Zhao, A. C. W. Creech, A. G. L. Borthwick, V. Venugopal, and T. Nishino, ‘Aerodynamic Analysis of a Two-Bladed Vertical-Axis Wind Turbine Using a Coupled Unsteady RANS and Actuator Line Model’, *Energies*, vol. 13, no. 4, Art. no. 4, Jan. 2020, doi: 10.3390/en13040776.
[20] V. Mendoza and A. Goude, ‘Validation of Actuator Line and Vortex Models Using Normal Forces Measurements of a Straight-Bladed Vertical Axis Wind Turbine’, *Energies*, vol. 13, no. 3, Art. no. 3, Jan. 2020, doi: 10.3390/en13030511.
[21] R. E. Sheldahl and P. C. Klimas, ‘Aerodynamic characteristics of seven symmetrical airfoil sections through 180-degree angle of attack for use in aerodynamic analysis of vertical axis wind turbines’, Sandia National Labs., Albuquerque, NM (USA), SAND-80-2114, Mar. 1981. doi: 10.2172/6548367.
[22] M. Drela, ‘XFOIL: An Analysis and Design System for Low Reynolds Number Airfoils’, University of Notre Dame, Jun. 1989. doi: 10.1007/978-3-642-84010-4_1.
[23] P. F. Melani, F. Balduzzi, G. Ferrara, and A. Bianchini, ‘Tailoring the actuator line theory to the simulation of Vertical-Axis Wind Turbines’, *Energy Convers. Manag.*, vol. 243, p. 114422, Sep. 2021, doi: 10.1016/j.enconman.2021.114422.

[24] P. F. Melani, F. Balduzzi, and A. Bianchini, ‘Simulating tip effects in vertical-axis wind turbines with the actuator line method’, *J. Phys. Conf. Ser.*, vol. 2265, no. 3, p. 032028, May 2022, doi: 10.1088/1742-6596/2265/3/032028.
[25] A. Bianchini *et al.*, ‘An Experimental and Numerical Assessment of Airfoil Polars for Use in Darrieus Wind Turbines: Part 1 — Flow Curvature Effects’, presented at the ASME Turbo Expo 2015: Turbine Technical Conference and Exposition, Aug. 2015. doi: 10.1115/GT2015-42284.
[26] A. Bianchini, F. Balduzzi, G. Ferrara, and L. Ferrari, ‘Aerodynamics of Darrieus Wind Turbines Airfoils: The Impact of Pitching Moment’, *J. Eng. Gas Turbines Power*, vol. 139, no. 4, Nov. 2016, doi: 10.1115/1.4034940.
[27] A. Bianchini, F. Balduzzi, G. Ferrara, and L. Ferrari, ‘Critical Analysis of Dynamic Stall Models in Low-Order Simulation Models For Vertical-Axis Wind Turbines’, *Energy Procedia*, vol. 101, pp. 488–495, Nov. 2016, doi: 10.1016/j.egypro.2016.11.062.
[28] L. A. Martínez-Tossas, M. J. Churchfield, and C. Meneveau, ‘A Highly Resolved Large-Eddy Simulation of a Wind Turbine using an Actuator Line Model with Optimal Body Force Projection’, *J. Phys. Conf. Ser.*, vol. 753, p. 082014, Sep. 2016, doi: 10.1088/1742-6596/753/8/082014.
[29] M. Cormier, P. Weihing, and T. Lutz, ‘Evaluation of the Effects of Actuator Line Force Smearing on Wind Turbines Near-Wake Development’, *J. Phys. Conf. Ser.*, vol. 1934, no. 1, p. 012013, May 2021, doi: 10.1088/1742-6596/1934/1/012013.
[30] ‘An Advanced Actuator Line Method for Wind Energy Applications and Beyond’, *AIAA SciTech Forum*. https://arc.aiaa.org/doi/10.2514/6.2017-1998 (accessed Jun. 13, 2022).
[31] ‘Optimal smoothing length scale for actuator line models of wind turbine blades based on Gaussian body force distribution - Martínez-Tossas - 2017 - Wind Energy - Wiley Online Library’. https://onlinelibrary.wiley.com/doi/10.1002/we.2081 (accessed May 23, 2022).
[32] ‘An Advanced Actuator Line Method for Wind Energy Applications and Beyond | AIAA SciTech Forum’. https://arc.aiaa.org/doi/10.2514/6.2017-1998 (accessed May 23, 2022).
[33] M. Schollenberger, T. Lutz, and E. Krämer, ‘Boundary Condition Based Actuator Line Model to Simulate the Aerodynamic Interactions at Wingtip Mounted Propellers’, in *New Results in Numerical and Experimental Fluid Mechanics XII*, Cham, 2020, pp. 608–618. doi: 10.1007/978-3-030-25253-3_58.
[34] P. F. Melani, F. Balduzzi, and A. Bianchini, ‘A Robust Procedure to Implement Dynamic Stall Models Into Actuator Line Methods for the Simulation of Vertical-Axis Wind Turbines’, *J. Eng. Gas Turbines Power*, vol. 143, no. 11, Sep. 2021, doi: 10.1115/1.4051909.
[35] P. F. Melani, F. Balduzzi, G. Ferrara, and A. Bianchini, ‘Development of a desmodromic variable pitch system for hydrokinetic turbines’, *Energy Convers. Manag.*, vol. 250, p. 114890, Dec. 2021, doi: 10.1016/j.enconman.2021.114890.
[36] G. Tescione, D. Ragni, C. He, C. J. Simão Ferreira, and G. J. W. van Bussel, ‘Near wake flow analysis of a vertical axis wind turbine by stereoscopic particle image velocimetry’, *Renew. Energy*, vol. 70, pp. 47–61, Oct. 2014, doi: 10.1016/j.renene.2014.02.042.
[37] D. Casteleim, G. Tescione, D. Ragni, C. Simao Ferreira, and M. Gaunaa, ‘Creating a benchmark of Vertical Axis Wind Turbines in Dynamic Stall for validating numerical models’, in *33rd Wind Energy Symposium*, 0 vols, American Institute of Aeronautics and Astronautics, 2015. doi: 10.2514/6.2015-0723.

[38] P. F. Melani, F. Balduzzi, L. Brandetti, C. J. Simão Ferreira, and A. Bianchini, 'An experimental and numerical analysis of the dynamic variation of the angle of attack in a vertical-axis wind turbine', presented at the TORQUE 2020, Delft, Netherlands, 2020.
[39] C. S. Ferreira, H. A. Madsen, M. Barone, B. Roscher, P. Deglaire, and I. Arduin, 'Comparison of aerodynamic models for Vertical Axis Wind Turbines', *J. Phys. Conf. Ser.*, vol. 524, p. 012125, Jun. 2014, doi: 10.1088/1742-6596/524/1/012125.
[40] E. Jost, L. Klein, H. Leipprand, T. Lutz, and E. Krämer, 'Extracting the angle of attack on rotor blades from CFD simulations', *Wind Energy*, vol. 21, no. 10, pp. 807–822, 2018, doi: 10.1002/we.2196.
[41] C. de Boor, *A Practical Guide to Splines*. New York: Springer-Verlag, 1978. Accessed: Nov. 23, 2020. [Online]. Available: https://www.springer.com/gp/book/9780387953663
[42] 'Correlation-Based Transition Modeling for Unstructured Parallelized Computational Fluid Dynamics Codes | AIAA Journal'. https://arc.aiaa.org/doi/10.2514/1.42362 (accessed May 23, 2022).
[43] L. A. Viterna and D. C. Janetzke, 'Theoretical And Experimental Power From Large Horizontal-Axis Wind Turbines', *NASA Tech. Memo.*, 1982.
[44] D. Marten *et al.*, 'Effects of airfoil's polar data in the stall region on the estimation of Darrieus wind turbines performance', *J Eng Gas Turbines Power*, vol. 139, no. 2, pp. 022606–9, 2016, doi: 10.1115/1.4034326.
[45] B. Massé, 'Description de deux programmes d'ordinateur pour le calcul des performances et des charges aérodynamiques pour les éoliennes à axe vertical', technical report IREQ-2379, 1981.
[46] R. E. Gormont, 'A Mathematical Model of Unsteady Aerodynamics and Radial Flow for Application to Helicopter Rotors', BOEING VERTOL CO PHILADELPHIA PA, May 1973. Accessed: Nov. 16, 2020. [Online]. Available: https://apps.dtic.mil/sti/citations/AD0767240
[47] P. G. Migliore, W. P. Wolfe, and J. B. Fanucci, 'Flow Curvature Effects On Darrieus Turbine Blade Aerodynamics', *J. Energy*, vol. 4, no. 2, pp. 49–55, 1980, doi: 10.2514/3.62459.
[48] P. F. Melani, P. Schito, and G. Persico, 'Experimental assessment of an ACL simulation tool for VAWTs', Riva del Garda (Italy), September 6-7, 2018.
[49] A. Bianchini, F. Balduzzi, L. Haack, S. Bigalli, B. Müller, and G. Ferrara, 'Development and Validation of a Hybrid Simulation Model for Darrieus Vertical-Axis Wind Turbines', presented at the ASME Turbo Expo 2019: Turbomachinery Technical Conference and Exposition, Nov. 2019. doi: 10.1115/GT2019-91218.
[50] P. Bachant, A. Goude, and M. Wosnik, 'Actuator line modeling of vertical-axis turbines', *ArXiv160501449 Phys.*, Sep. 2018, Accessed: Jun. 16, 2020. [Online]. Available: http://arxiv.org/abs/1605.01449
[51] V. Mendoza, P. Bachant, C. Ferreira, and A. Goude, 'Near-wake flow simulation of a vertical axis turbine using an actuator line model', *Wind Energy*, vol. 22, no. 2, pp. 171–188, 2019, doi: 10.1002/we.2277.
[52] 'Two-equation eddy-viscosity turbulence models for engineering applications | AIAA Journal'. https://arc.aiaa.org/doi/abs/10.2514/3.12149?journalCode=aiaaj (accessed Jul. 06, 2022).
[53] F. Balduzzi, A. Bianchini, G. Ferrara, and L. Ferrari, 'Dimensionless numbers for the assessment of mesh and timestep requirements in CFD simulations of Darrieus wind turbines', *Energy*, vol. 97, pp. 246–261, Feb. 2016, doi: 10.1016/j.energy.2015.12.111.

[54] ‘A Comparison of Actuator Disk and Actuator Line Wind Turbine Models and Best Practices for Their Use’, *Aerospace Sciences Meetings*. https://arc.aiaa.org/doi/10.2514/6.2012-900 (accessed Jul. 04, 2022).